



# Cross-Shelf Exchange in the Southwestern Atlantic Shelf: Climatology and Extreme Events

Giuliana Berden<sup>1,2,3\*</sup>, Alberto R. Piola<sup>1,2,3,4</sup> and Elbio D. Palma<sup>2,5</sup>

<sup>1</sup> Facultad de Ciencias Exactas y Naturales, Universidad de Buenos Aires, Buenos Aires, Argentina, <sup>2</sup> Consejo Nacional de Investigaciones Científicas y Técnicas (CONICET), Buenos Aires, Argentina, <sup>3</sup> Departamento Oceanografía, Servicio Hidrografía Naval, Buenos Aires, Argentina, <sup>4</sup> Unidad Mixta Internacional - Instituto Franco-Argentino Sobre Estudios del Clima y sus Impactos, Buenos Aires, Argentina, <sup>5</sup> Departamento de Física, Universidad Nacional del Sur and Instituto Argentino de Oceanografía/CONICET, Bahía Blanca, Argentina

## OPEN ACCESS

### Edited by:

William Savidge,  
University of Georgia, United States

### Reviewed by:

Ryan McCabe,  
National Oceanic and Atmospheric  
Administration (NOAA), United States  
Dorleta Orue-Echevarria,  
Institut de Ciències del Mar (CSIC),  
Spain

### \*Correspondence:

Giuliana Berden  
giuliberden@gmail.com

### Specialty section:

This article was submitted to  
Coastal Ocean Processes,  
a section of the journal  
Frontiers in Marine Science

**Received:** 14 January 2022

**Accepted:** 07 February 2022

**Published:** 09 March 2022

### Citation:

Berden G, Piola AR and Palma ED  
(2022) Cross-Shelf Exchange in the  
Southwestern Atlantic Shelf:  
Climatology and Extreme Events.  
*Front. Mar. Sci.* 9:855183.  
doi: 10.3389/fmars.2022.855183

The variability and drivers of the cross-shelf exchanges between the Southwestern Atlantic shelf and the open ocean from 30 to 40°S are analyzed using a high-resolution ocean model reanalysis at daily resolution. The model's performance was first evaluated using altimetry data, and independent mooring and hydrographic data collected in the study area. Model transports are in overall good agreement with all other estimates. The record-mean (1993–2018) cross-shore transport is offshore,  $2.09 \pm 1.60$  Sv. 73% of the shelf-open ocean exchange occurs in the vicinity of Brazil-Malvinas Confluence (~38°S) and 20% near 32°S. This outflow is mostly contributed by northward alongshore transport through 40°S (63%) and the remaining by southward transport through 30°S (37%). The cross-shore flow presents weak seasonal variations, with a maximum in austral summer, and high variability at subannual and weekly time scales. The latter is mainly associated with abrupt wind changes generated by synoptic atmospheric systems. Alongshore wind variations set up sea-level changes in the inner shelf which in turn drive large anomalies in the associated geostrophic alongshore flow. The difference in inner shelf sea-level anomalies at 30 and 40°S is a good indicator of cross-shelf exchange at seasonal and shorter time scales. Episodes of extreme offshore transport that reach up to 9.45 Sv and last about 2 days are driven by convergence of these alongshore flows over the shelf. Large exports of shelf waters lead to freshening of the upper open ocean as revealed by *in-situ* and satellite observations. In contrast, onshore extreme events drive open ocean water intrusions of up to 6.53 Sv and last <4 days. These inflows, particularly the subtropical waters from the Brazil Current, induce a substantial salinification of the outer shelf.

**Keywords:** cross-shelf exchange, western boundary current, Brazil-Malvinas Confluence, continental shelf, high frequency variability, extreme events

## 1. INTRODUCTION

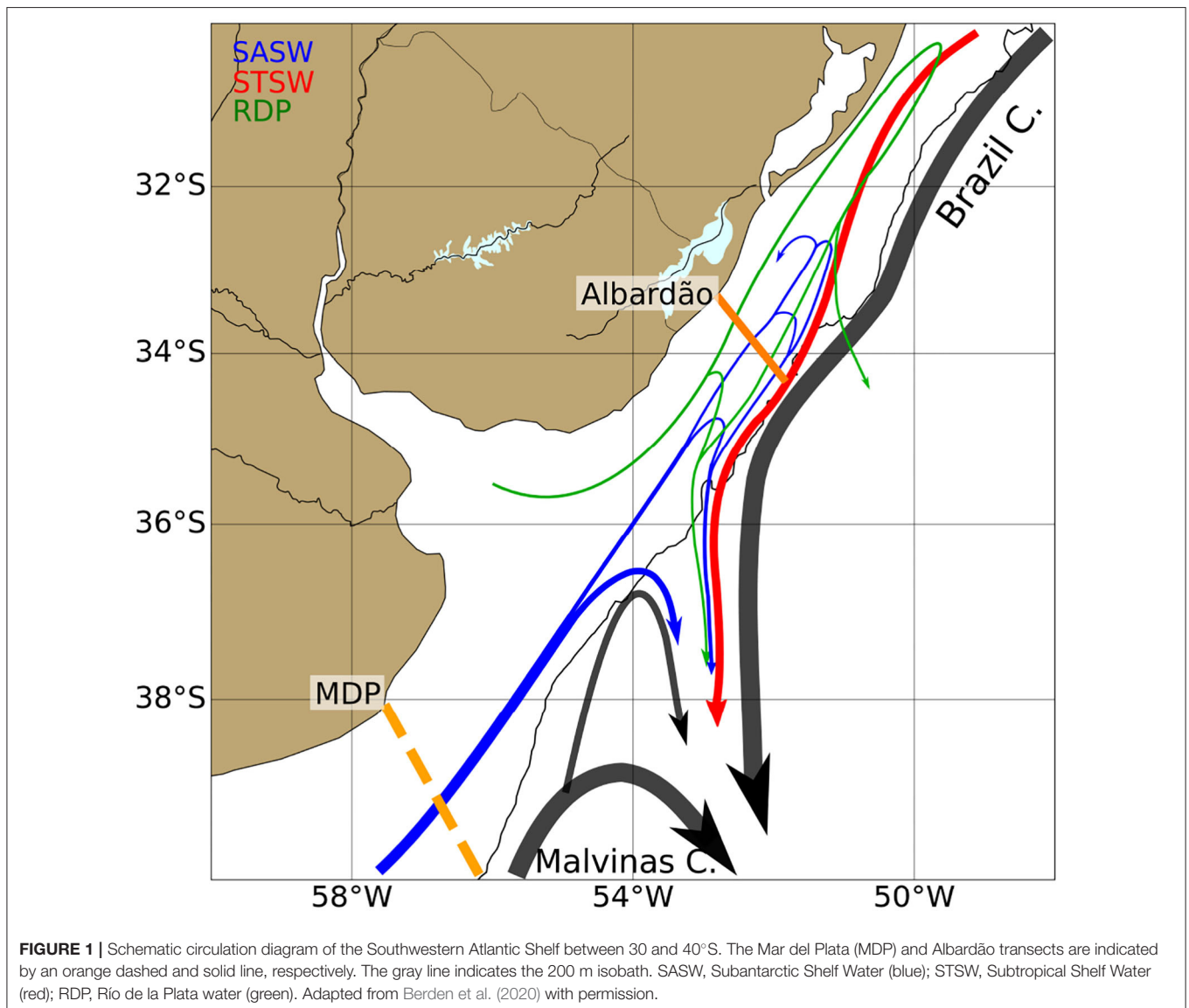
Continental shelves account for <10% of the global ocean surface, yet they host 20–30% of the ocean's primary production (de Haas et al., 2002) and 90% of the global fish catch (Gattuso et al., 1998). In addition, continental shelves play a key role in the biogeochemical cycling of the ocean due to the continental discharge of organic matter and nutrients. Consequently, 80% of organic carbon

is buried in continental shelves (Rabouille et al., 2001; Chen et al., 2003) and these are important sites for denitrification (Christensen et al., 1987; Rabouille et al., 2001). The Southwestern Atlantic Shelf (SWAS) hosts one of the most productive marine ecosystems of the southern hemisphere due to the supply of nutrients from continental discharge, shelf currents, and open ocean sources. The high primary productivity over the shelf and its subsequent fate might have a significant biogeochemical impact on the open ocean.

Bounding the SWAS, the Malvinas Current (MC) flows northeastward carrying relatively low-salinity, cold and nutrient-rich waters from the Antarctic Circumpolar Current. The MC reaches approximately 38°S where it collides with the Brazil Current (BC), which advects warm and salty waters southward (Gordon and Greengrove, 1986, **Figure 1**). The latitudinal position of the Brazil/Malvinas Confluence (BMC) varies seasonally, shifting southward

during the austral fall and northward during the austral spring (Combes and Matano, 2014a). There is also a southward shift of the BMC position in the past decades associated with a longer-term oscillation (Lumpkin and Garzoli, 2011).

Diluted subantarctic waters referred to as Subantarctic Shelf Waters (SASW) enter the SWAS near 54°S (Piola et al., 2018). These cold, relatively low-salinity (~33.8) and nutrient-rich waters flow northward and reach the Southern Brazilian Shelf at 34°S to 32°S, where they meet a southwestward flow of warm-salty Subtropical Shelf Waters (STSW), forming the Subtropical Shelf Front (STSF, Piola et al., 2000). The STSF is a subsurface front capped by low-salinity waters derived from the Río de la Plata (RDP). The RDP is the major contributor of continental nutrients and organic matter to the central portion of the SWAS (Braga et al., 2008; see Figure 1 in Piola et al., 2018; Bordin et al., 2019; Berden et al., 2020). On average, the RDP discharges around 25,000  $m^3 \cdot s^{-1}$  of freshwater over the shelf



(Borús et al., 2017). From April to September south of 30°S the continental shelf is dominated by southwesterly winds, while northeasterly winds prevail from October to March (e.g., Matano et al., 2014). These seasonal reversals in alongshore winds have a profound effect on the shelf circulation, leading to northeastward extensions of the RDP low salinity waters to 28°S in fall-winter, and retraction to 32°S in spring-summer (Piola et al., 2000, 2005). Direct current meter observations near 40°S indicate a mean northeastward transport of SASW of 2.65 Sv, with large variability, including transport reversal events lasting a few days, which are closely associated with alongshore winds variability (Lago et al., 2021). Numerical models suggest that the transport over the shelf is modulated by the intensity of the MC, which sets up the cross-shore pressure gradient (Matano et al., 2010). However, altimetry-derived velocity fields and more recent numerical simulations indicate this influence is limited to a few tens of kilometers over the outer shelf (Combes and Matano, 2018; Lago et al., 2021). The influence of the tides north of 39°S is very limited except in the inner portion of the RDP (Palma et al., 2004).

Strong western boundary currents (WBCs), including the BC and the MC, are thought to act as barriers to exchanges between the shelf and the open ocean (Roughan et al., 2011; Franco et al., 2017; Malan et al., 2020). However, *in-situ* and satellite observations, and numerical simulations indicate that the BMC is an effective conduit of shelf waters toward the deep adjacent ocean (Guerrero et al., 2014; Matano et al., 2014; Berden et al., 2020). Synoptic hydrographic observations suggest that the STSF is nearly density-compensated (Piola et al., 2000, 2008) allowing the necessary baroclinicity for cross-isobaths exchanges (Berden et al., 2020). The slight changes in isopycnal depth on either side of the STSF and its partial cross-shore orientation allow cross-isobath movements suggesting the STSF may be a path of export of shelf waters to the open ocean. Combes et al. (2021) suggest that between 22.2 and 35°S the mean cross-isobath transport is modulated by the bathymetry and its variability is determined by the local wind and the internal variability of the BC. In addition, onshore intrusions of South Atlantic Central Waters (SACW) in the bottom layer of the outer shelf north of the BMC have been reported in several studies (Braga et al., 2008; Möller et al., 2008; Piola et al., 2008; Palma and Matano, 2009; Berden et al., 2020). These SACW intrusions are a significant nutrient source to the shelf region (e.g., Ciotti et al., 1995 and references therein).

Analyses of *in-situ* observations provided a synoptic characterization of the water exchange between the SWAS and the open ocean (Berden et al., 2020) estimating an offshore transport of 3.44 Sv between 32.1 and 37.7°S. Analyses of altimetry data indicate a maximum off-shelf transport in January–June between 35 and 38°S, and a minimum in July to December (Strub et al., 2015). Matano et al. (2010) and Combes and Matano (2014b) study the interaction between the WBCs and the shelf in the South Brazil Bight and Patagonia based on numerical models. North of 29°S, the circulation is driven by the interaction between intrusions of the BC over the middle and outer-shelf and upwelling favorable wind stress in the inner-shelf. Between 30 and 40°S, the STSF seems to be a preferential path for the ejection of shelf waters. Matano et al. (2014) use 10-day

averaged outputs from a high-resolution model (1/24°) to analyze the exchanges of shelf-waters focusing on the sea surface salinity variability. The model suggests that low-salinity waters of the RDP are exported in the vicinity of the BMC. A Lagrangian particle analysis with a similar model indicates that the export of SASW occurs primarily along two different paths (Franco et al., 2018). The waters following a fast path (<2 months) are exported near the BMC and those following a slow path (>130 days), flow northward over the shelf beyond the latitude of the BMC, describe a cyclonic loop near 32°S and subsequently follow the shelf-break southward to the BMC. Likewise, other numerical simulations (1/12°, 10-day average) suggest that the location of the BMC determines the position of the largest offshore transport, but not its magnitude (Combes and Matano, 2018). Recent analyses based on a high-resolution nested model (1/36°, 5-day average) indicate an offshore transport of ~1.6 Sv between 35 and 25.2°S (Combes et al., 2021).

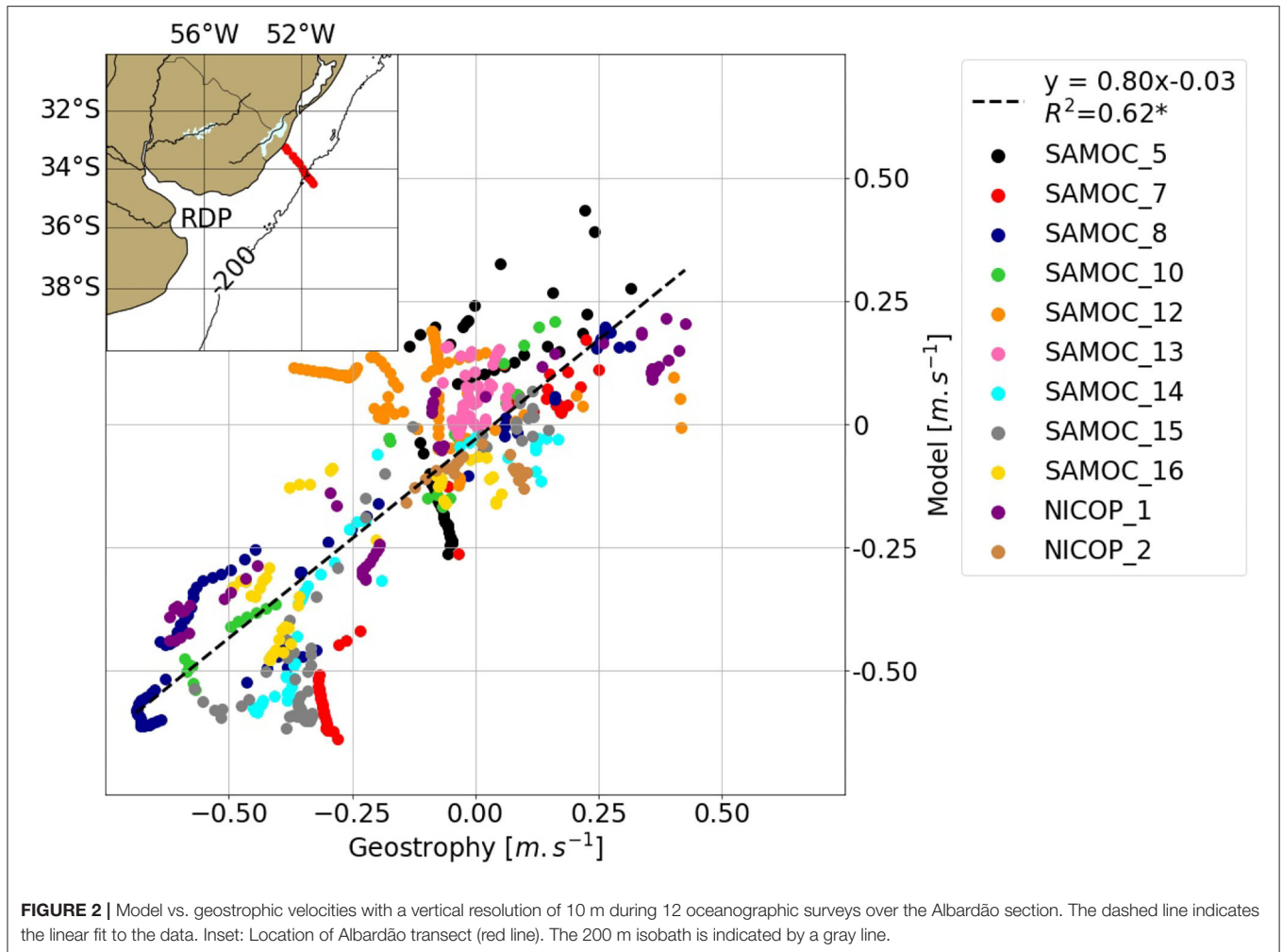
In this article, we extend previous studies analyzing the export of shelf waters to the open ocean between 30 and 40°S and its time and space variability using daily outputs from a global high-resolution ocean model reanalysis. Given the recent observational evidence of large-amplitude alongshore transport fluctuations at a synoptic time scale near 40°S (Lago et al., 2021) we also analyze the model results to determine if such changes may impact the offshore transport. The daily resolution of the reanalysis allows us to study the temporal variability at high frequencies, which has not been discussed hitherto.

## 2. DATA AND METHODS

### 2.1. Reanalysis

#### GLOBAL\_REANALYSIS\_PHY\_001\_030

This study is based on the analysis of the Copernicus Marine Environment Monitoring Service (CMEMS) global ocean reanalysis (GLORYS12V1) during 1993–2018. GLORYS12V1 is based on the NEMOv3.1 ocean model, described in Madec et al. (2017). The model is driven at the surface by the ERA-interim atmospheric reanalysis from the European Centre for Medium-Range Weather Forecasts. Satellite-derived along-track sea level anomaly (SLA, Pujol et al., 2016), sea surface temperature (SST) from NOAA's Optimum Interpolation Sea Surface temperature (0.25°, Reynolds et al., 2007), sea ice concentration from CERSAT and *in situ* vertical profiles of temperature (T) and salinity (S) from the CORA4.1 database (Cabanes et al., 2013) are jointly assimilated. The assimilation procedure employs a reduced-order Kalman filter with a 3D multivariate modal decomposition of the background error. The assimilation procedure includes an adaptive-error estimate and a localization algorithm. In addition, a 3D-VAR scheme corrects for the slowly-evolving large-scale biases in temperature and salinity (Lellouche et al., 2018). The reanalysis does not incorporate tidal forcing. The model output is provided daily on a standard regular grid at 1/12° (~8 km) and on 50 standard vertical levels, with 22 levels in the upper 100 m. Consequently, the vertical resolution is 1 m at the surface, decreases to 33 m at the bottom of the continental shelf (200 m), and reaches 450 m near the bottom in the deep ocean (5,700 m).



## 2.2. In-situ Data

To evaluate the model performance, the model was compared with *in-situ* data collected during 12 hydrographic surveys over a cross-shelf transect off southern Brazil, hereafter referred to as the Albardão transect (**Figure 2** and **Table 1**). The data consists of high-resolution, cross-shore sections of conductivity-temperature-depth (CTD) profiles occupied between August 2003 and October 2018. In addition, the alongshore volume transport between the coast and the 200 m isobath near 39°S (hereafter referred to as the MDP transect, location shown by the orange dashed line in **Figure 1**) has been recently estimated, hereafter referred to as  $T_{Obs}$ , based on direct current observations during 11 months from December 2014 to November 2015. Details of these transport estimates are provided in Lago et al. (2021). Note that the *in-situ* observations used herein were not assimilated to the ocean reanalysis.

## 2.3. Satellite Data

The altimetry data (sea level anomalies and associated geostrophic currents) used in this analysis were the delayed-time merged all satellites Global Ocean Gridded SSALTO/DUACS Sea

**TABLE 1** | Hydrographic surveys along the Albardão transect.

Cruise	Dates	Vessel	Country
NICOP_1	26–27 August 2003	Puerto Deseado	Argentina
NICOP_2	9–10 February 2004	Antares	Brazil
SAMOC_5	5–6 July 2011	Puerto Deseado	Argentina
SAMOC_7	9 July 2012	Puerto Deseado	Argentina
SAMOC_8	10 Dec 2012	Alpha-Crucis	Brazil
STSF	7–8 October 2013	Puerto Deseado	Argentina
SAMOC_10	14 October 2014	Puerto Deseado	Argentina
SAMOC_12	17–18 September 2016	Alpha-Crucis	Brazil
SAMOC_13	29 October 2016	Puerto Deseado	Argentina
SAMOC_14	29–30 September 2017	Puerto Deseado	Argentina
SAMOC_15	25 April 2018	Alpha-Crucis	Brazil
SAMOC_16	26 October 2018	Puerto Deseado	Argentina

Surface Height L4 product from Copernicus Marine (Pujol et al., 2016). The gridded product has a spatial resolution of  $1/4^\circ$  on a regular grid and a daily temporal resolution.

## 2.4. Wind Data

Wind stress data was obtained from the ERA5 global atmospheric reanalysis (Hersbach et al., 2020), which covers 1979–2022, produced by the European Center of Middle-range Weather Forecast (ECMWF). This product is available hourly over a regular grid of  $1/4^\circ$ . Daily averages were used in this work.

## 2.5. Methods

Since the WBCs may act as barriers to exchanges between the shelf and the open ocean, the possible impact of the BC and MC intensity is studied. The analysis of the BC variability is based on the depth-averaged model velocity in the upper 0–200 m at  $34.5^\circ\text{S}$  projected in the local along-slope direction (orientation of  $36^\circ$  from the true north). Likewise, the MC velocity was defined at  $42^\circ\text{S}$ , where the model velocity is projected to  $45^\circ$  from the true north. Since the BC presents substantial mesoscale variability (see Chidichimo et al., 2021), it is difficult to determine its precise position in the cross-shore direction along  $34.5^\circ\text{S}$  in the daily model outputs. Therefore, the position of the current was determined using the mean velocity field between 1993 and 2018 considering the current as a uniform flow with intensity  $>10\text{ cm}\cdot\text{s}^{-1}$ . Once the position of the current is established, the along-slope velocity component is averaged horizontally to obtain a single velocity time series. The same procedure is followed to determine the MC intensity. The sensitivity of the definition of both currents to changes in the velocity threshold and depth over which the velocity is integrated was analyzed (Supplementary Figure 1). The resulting velocity magnitude is not significantly sensitive to changes in depth of integration considering a range of 200–400 m. Although the velocity magnitude displays variations associated with changes in the threshold used to define the BC and MC, tested in the range of  $5\text{--}20\text{ cm}\cdot\text{s}^{-1}$ , these changes are small and the resulting velocities are highly correlated ( $R^2 > 0.85^*$ ). The significance of the statistical correlations was calculated at a 95% confidence level. Hereafter, significant correlations are indicated with an asterisk (\*), and correlations with  $R^2 < 0.15$  will not be addressed. In addition, the BMC location was analyzed as a possible driver of cross-shelf exchange. The position of the BMC is determined daily as the latitude where the  $10^\circ\text{C}$  isotherm at 200 m intersects the 1,000 m isobath (Goni and Wainer, 2001; Matano et al., 2014).

## 3. RESULTS AND DISCUSSION

### 3.1. Evaluation of Model Performance

In this section, we evaluate the model's ability to capture the patterns of the shelf circulation and its time variability. To this end, we compare the model outputs with available *in-situ* and satellite observations.

#### 3.1.1. Currents

The currents extracted from the model over the continental shelf were first compared with *in-situ* data collected in the Albardão transect (Figure 2). Alongshore geostrophic velocities relative to the sea surface were estimated from the hydrographic data with a vertical resolution of 10 m. Absolute velocities were then computed by adjusting the relative geostrophic profiles

to the surface geostrophic velocity derived from the gridded altimetry data. Model velocities were projected in the alongshore direction and low-passed filtered with a 5-day window. Model and observations are in relatively good agreement based on the linear correlation ( $R^2 = 0.62^*$ ).

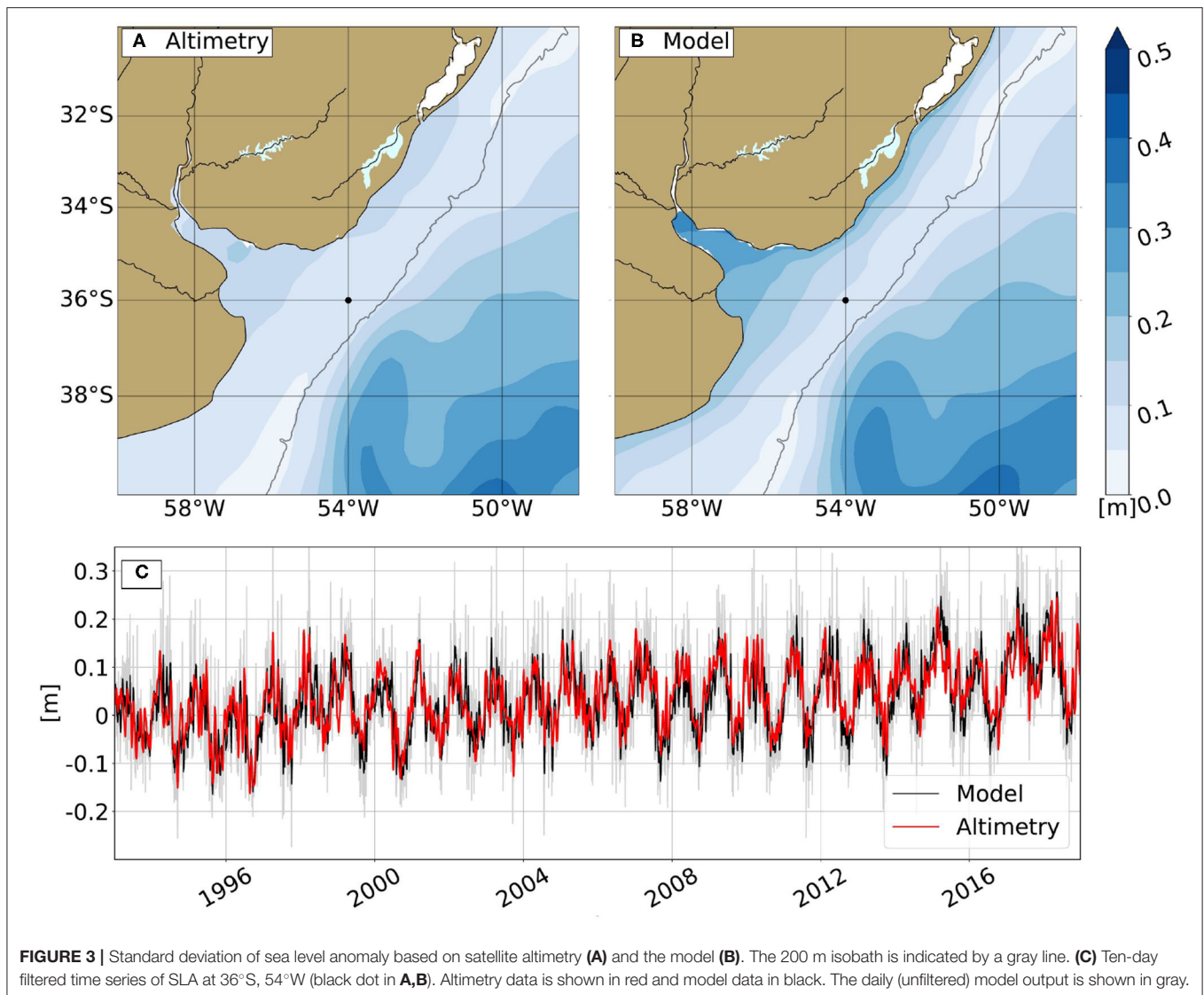
#### 3.1.2. Comparison With Satellite Altimetry

To further evaluate the model performance, we compared the standard deviation of the sea level anomaly (SLA) from the model and the gridded satellite data. It is important to note that the model assimilates altimetry derived along-track sea level. The spatial structures of the standard deviation of SLA (Figure 3) are very similar at offshore locations and present the largest differences over the RDP estuary and coastal regions northeast of the RDP mouth. To analyze the temporal evolution of SLA we selected a location on the mid-shelf close to the climatological latitude of the BMC ( $36.9^\circ\text{S}$ ), which is a preferential location of export of shelf-waters to the open ocean (black dot in Figures 3A,B). The 10-day filtered time series of SLA shows a significant correlation ( $R^2 = 0.72^*$ ) between the model and the altimeter data. This correlation decreases considering daily data ( $R^2 = 0.50^*$ ) because the model output contains more high-frequency variability than the altimeter data. These differences between altimetry and model results are expected because of the comparatively poor space and time resolution of the altimeter data. Although the gridded altimetry product is available daily, the most frequent (Jason 3) revisits occur at 10-day intervals. Therefore, the gridded altimetric product has an effective spatial and temporal resolution of 280 km and 21 days (see Figures 2B, 3 in Ballarotta et al., 2019) and cannot appropriately resolve estuarine and nearshore features, nor small mesoscale features (Pujol et al., 2016) generated by the model's internal dynamics.

#### 3.1.3. Comparison With *in-situ* Alongshore Transports

Alongshore transport over the MDP transect between the coast and the 200 m isobath near  $39^\circ\text{S}$  was recently estimated by Lago et al. (2021) using *in-situ* data ( $T_{Obs}$ ). The analyses of Lago et al. (2021) reveal the barotropic nature of the circulation and a close agreement between geostrophic and direct transport estimates. To evaluate the model performance, we computed the alongshore component of model transport across the same line, hereafter referred to as  $T_{Model}$  (Figure 4). The time-averaged  $T_{Obs}$  is 2.68 Sv and its standard deviation is 2.13 Sv. Meanwhile,  $T_{Model}$  presents lower mean and standard deviations; 2.13 and 1.32 Sv, respectively. In addition, flow reversal events were analyzed by Lago et al. (2021). Particularly, an event observed in early May 2015 shows a flow reversal from  $-2.57$  to  $5.84$  Sv in  $T_{Obs}$  and from  $-1.46$  to  $5.15$  Sv in  $T_{Model}$ .

$T_{Model}$  explains 79% of the variance of  $T_{Obs}$  (Figure 4C). However, the mean difference of 0.55 Sv represents a relative error of  $0.55\text{ Sv}/2.68\text{ Sv} = 0.20$ , or 20% less than the observed transport.  $T_{Model}$  has less energy than  $T_{Obs}$  at periods shorter than  $\sim 30$  days. However, both transport time series present peaks at similar frequencies at around 5.8, 7.4, 10, 16, 28, and 85 days (Figure 4D).  $T_{Obs}$  displays higher energy in almost all peaks except at 85 days where both model and *in-situ* transports



are in much better agreement. Hence, the model reproduces the regional dynamics but it contains lower energy at shorter periods.

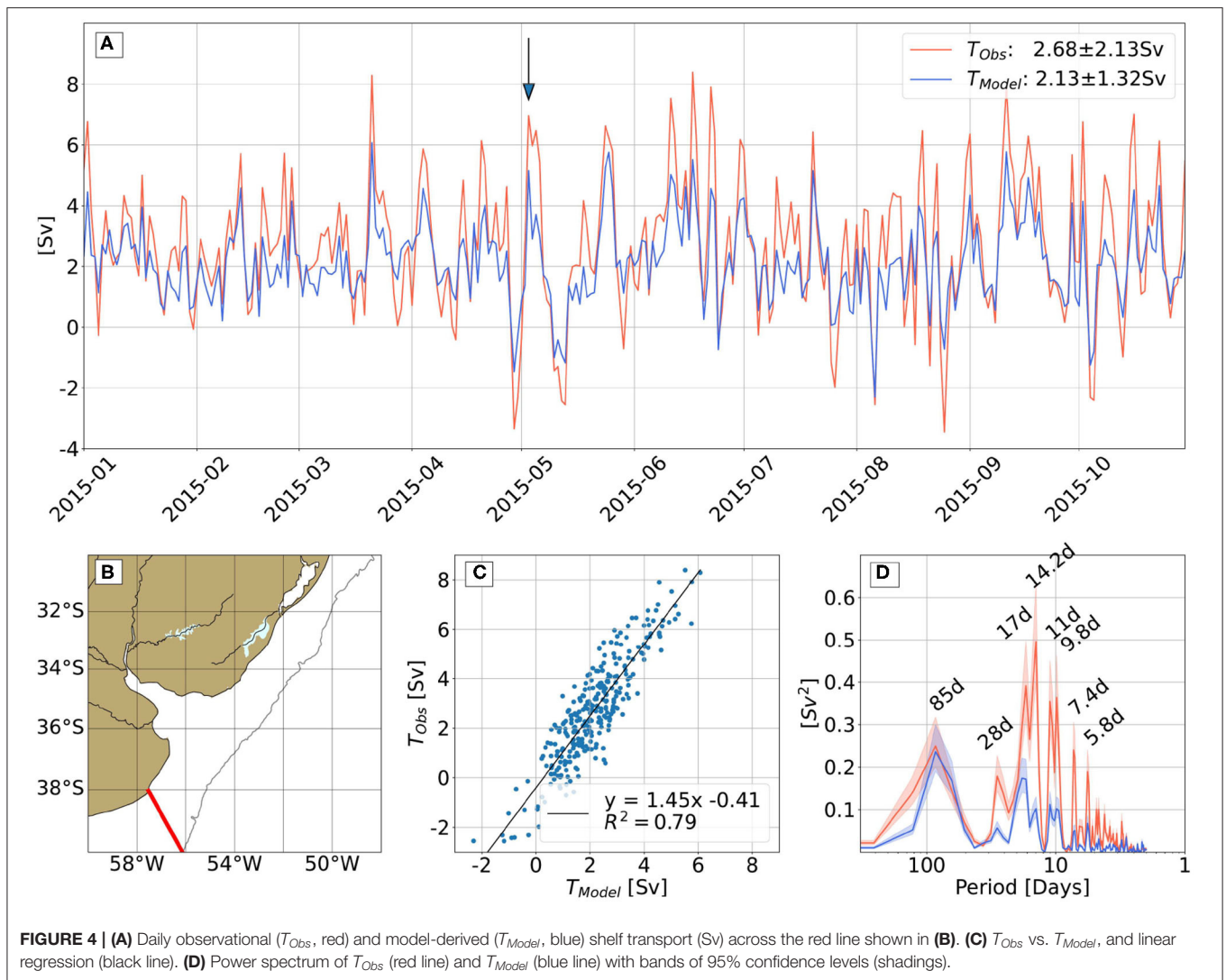
Additionally, Lago et al. (2021) estimated the alongshore transport using altimeter data ( $T_{Sat}$ ). Their mean  $T_{Sat}$  is  $2.42 \pm 0.64$  Sv, thus matching quite well the  $2.13 \pm 1.32$  Sv from the model during the same period. Since the model assimilates along-track altimeter sea level anomaly, this agreement is not surprising.

### 3.2. Cross-Shore Transport Variability

To study the cross-shore transport between 30 and 40°S and its temporal and spatial variability, the 200 m isobath was divided into 20 zonal bands each spanning 0.5° of latitude (Figure 5). The time-averaged offshore transport through each outer shelf segment was estimated as the sum of the transports entering through the northern and southern boundaries of each zonal band. The total offshore transport between 30 and 40°S, hereafter referred to as  $T_{Cross}$  (Figure 6C), is defined as the sum of the

transports entering through the northern boundary at 30°S ( $T_N$ , positive southward, i.e., entering the domain; Figure 6A) and the southern boundary at 40°S ( $T_S$ , positive entering the domain; Figure 6B). We estimated the changes in the volume of shelf water based on the changes in the model-derived SLA. The resulting rate of daily volume change has a standard deviation of 0.16 Sv, which is an order of magnitude smaller than the typical daily mass convergence between 30 and 40°S. Thus, we assumed the mass storage plays a minor role in the cross-shore transports estimated based on mass conservation. We also investigate extreme events which are defined as those periods when the transport is higher/lower than the record-mean  $\pm 2$  standard deviations. In addition, possible physical mechanisms modulating the variability of the cross-shore transport such as the intensity of the BC and the MC, the BMC location, the alongshore transport variability, and the winds are analyzed.

The variability of the shelf transports ( $T_N$ ,  $T_S$ , and  $T_{Cross}$ ) can be caused by circulation changes occurring on a variety of



time scales. Thus, it is useful to split the model-derived transport variability by filtering the daily transport signals as follows:

$$T = T_{mean} + T_{weekly} + T_{subannual} + T_{seasonal} + T_{interannual} \quad (1)$$

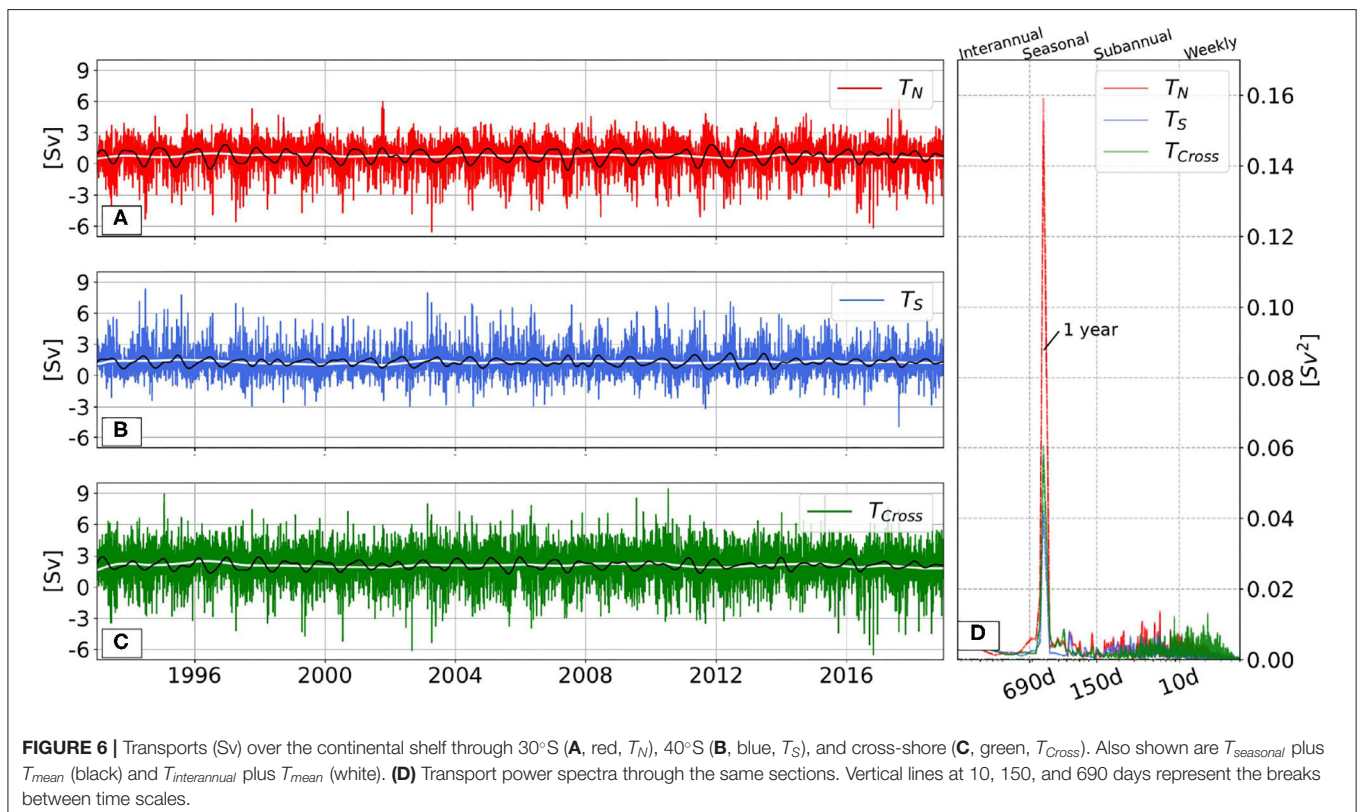
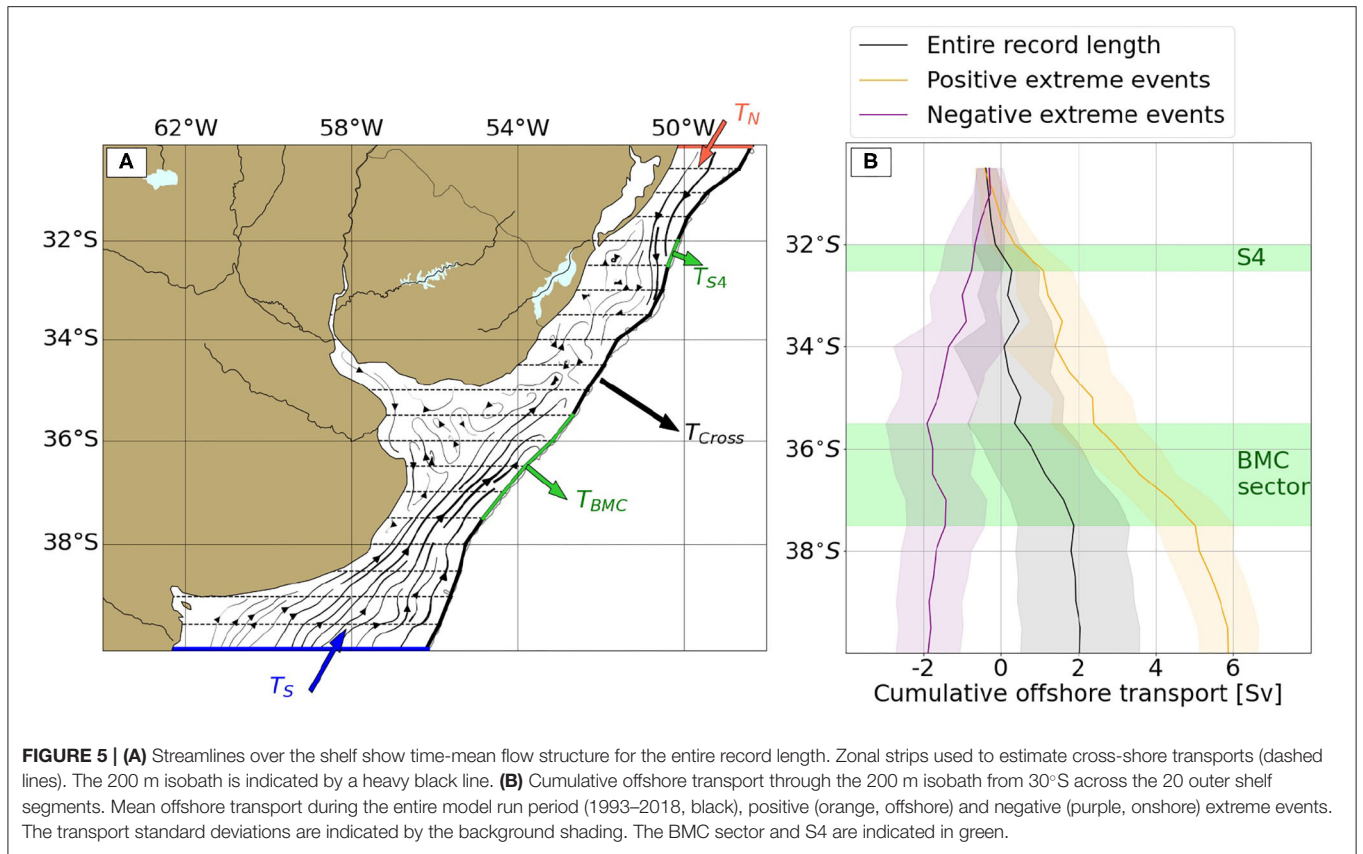
where  $T_{mean}$  is the record-mean transport and  $T_{weekly}$ ,  $T_{subannual}$ ,  $T_{seasonal}$ , and  $T_{interannual}$  are associated with weekly (<10 days), subannual (10 days–5 months), seasonal (5–23 months), and interannual (>23 months) time scales, respectively (Hirschi et al., 2007). To compute each component the daily transport time series is filtered with a Butterworth window of order 5. The weekly scale is included to study the high-frequency variability, which is particularly relevant to understand the extreme offshore transport anomaly events. **Table 2** shows the standard deviation of each transport and for each of the above-defined time scales. The larger variability is concentrated on the subannual and weekly time scales, with the latter being the largest. Although the transport power spectrum shows a marked peak around 1 year (2.7–9.2% of energy), there is a substantial amount of energy (>85%) distributed in the high

frequencies (subannual and weekly), without a characteristic frequency (**Figure 6D**).

### 3.2.1. Mean, and Low-Frequency Variability (Interannual and Seasonal)

The record-length mean offshore transport [mean  $\pm$  1 standard deviation] between 30 and 40°S ( $T_{Cross}$ ) is  $2.09 \pm 1.60$  Sv (**Table 3**). Sixty-three percent ( $1.31 \pm 1.16$  Sv) of  $T_{Cross}$  is contributed by  $T_S$  and the remaining 37% ( $0.78 \pm 1.36$  Sv) by  $T_N$ . The contribution of continental discharge from the RDP is <1% of the offshore transport variability. Previous estimates of the mean off-shelf transport based on the analyses of a high-resolution regional model show a mean offshore transport of 1.21 Sv between 34 and 38°S (Matano et al., 2014). This is in relatively good agreement with the GLORYS12V1 offshore transport computed over the same latitude range ( $1.72 \pm 1.35$  Sv).

The offshore flow across the 200 m isobath is not uniform. Most of the flow ( $1.53 \pm 0.74$  Sv or 73%, **Table 3**) occurs in the vicinity of the BMC (between 35.5 and 37.5°S, hereinafter





referred to as “BMC sector”) and about 20% of  $T_{Cross}$  occurs in the vicinity of 32°S ( $0.42 \pm 0.31$  Sv, hereinafter referred to as “S4”; **Figure 5**).

The record-mean circulation pattern (**Figure 5A**) is in agreement with Matano et al. (2014), Combes and Matano (2018), and Combes et al. (2021). It shows that water entering from the north of the domain is exported through S4 while water entering from the south of the domain is mostly exported in the vicinity of BMC. Transport variations at the interannual scale present a low standard deviation ( $<0.15$  Sv, **Table 2**) and display similar spectral amplitudes throughout this time scale. The preferential export routes at interannual time scales do not show significant relationships with  $T_N$  and  $T_S$ .

Although  $T_N$ ,  $T_S$ , and  $T_{Cross}$  do not show high standard deviation at the seasonal time scales (**Table 2**), they all have high spectral energy around 1 year (**Figure 6D**). The annual cycle of  $T_N$  presents a minimum transport ( $<0.43 \pm 0.40$  Sv) from April to July and a maximum transport ( $1.26 \pm 0.34$  Sv) in October (**Figure 7**), in agreement with Strub et al. (2015) and Combes and Matano (2018). In contrast,  $T_S$  presents a maximum from April to July ( $>1.46 \pm 0.35$  Sv) and a minimum ( $0.95 \pm 0.31$  Sv) in October. The above-described annual cycle of  $T_S$  is in good agreement with Strub et al. (2015) and Combes and Matano (2018) and the altimetry-derived transport through a cross-shelf section at around 39°S recently reported by Lago et al. (2021). The annual cycles of  $T_N$  and  $T_S$  are partially compensated. Consequently,  $T_{Cross}$  shows a maximum of  $2.40 \pm 0.37$  Sv in January and a minimum of  $1.74 \pm 0.34$  Sv in June.

When analyzing the predominant export locations, the cross-shore transport through the BMC sector ( $T_{BMC}$ ) presents subtly

higher seasonal variability than  $T_{Cross}$  and similar spectral energy concentrated around one year (**Supplementary Figure 2**). The annual cycle of  $T_{BMC}$  (**Figure 7B**) shows a maximum ( $1.82 \pm 0.49$  Sv) in January and a minimum ( $1.20 \pm 0.37$  Sv) in August. The cross-shore transport through S4 ( $T_{S4}$ ) also presents an annual cycle with a maximum ( $0.54 \pm 0.18$  Sv) in October and a minimum ( $0.28 \pm 0.12$  Sv) in June. At the seasonal scale, significant and positive correlations between  $T_{Cross}$  and  $T_{BMC}$  ( $0.55^*$ ) and between  $T_{Cross}$  and  $T_{S4}$  ( $0.77^*$ ) are observed (**Figure 8J**). Most of the variability of  $T_{S4}$  is associated with  $T_N$  ( $R^2 = 0.71^*$ , not shown). However,  $T_{BMC}$  presents no relationship with  $T_S$  (not shown). The seasonal component of  $T_S$  presents a negative correlation with  $T_{S4}$  ( $R^2 = 0.30^*$ , not shown). However, it is difficult to identify a physical process that may explain this correlation.

The climatology of the vertical temperature and salinity structure of the outer shelf averaged over the BMC sector is shown in **Figure 7C**. Note that on average the transport through this sector is offshore (positive) throughout the year (**Figure 7B**). Low salinity waters ( $S < 33.5$ ), characteristic of shelf waters diluted by the RDP discharge, are present in the upper layer ( $z < 25$  m) throughout the year, except in winter (JJA) when saltier and colder waters ( $S \sim 33.8$ ,  $< 11^\circ\text{C}$ ), associated with SASW are observed. Below this near-surface layer, waters with salinities between 33.8 and 35 are observed throughout the year. These waters represent mixtures of SASW with TW (Tropical Waters)/SACW. The salinity and temperature maxima observed during April–May and November are associated with a higher proportion of TW/SACW. On average the transport through S4 is also offshore (positive) throughout the year (**Figure 7B**). The vertical temperature and salinity structures are shown in **Figure 7D**. Low-salinity ( $S < 33.5$ ) RDP waters are exported in the upper layer ( $z < 25$  m) during July–October. During this period, at about 60 m depth, waters are warmer ( $> 19^\circ\text{C}$ ) and saltier ( $> 34$ ) than in the upper layer. The rest of the year, saltier waters ( $S > 34$ ) with surface temperatures ranging from  $25.6^\circ\text{C}$  in March to  $16.4^\circ\text{C}$  in July associated with STSW are exported to the open ocean through S4.

### 3.2.1.1. Drivers of Low Frequency (Interannual and Seasonal) Cross-Shore Transport Variability

In this section, we analyze the physical mechanisms driving offshore transport at low frequencies. At interannual scales,

**TABLE 2** | Standard deviation of transport (Sv) through selected sections, estimated over the entire model period (1993–2018).

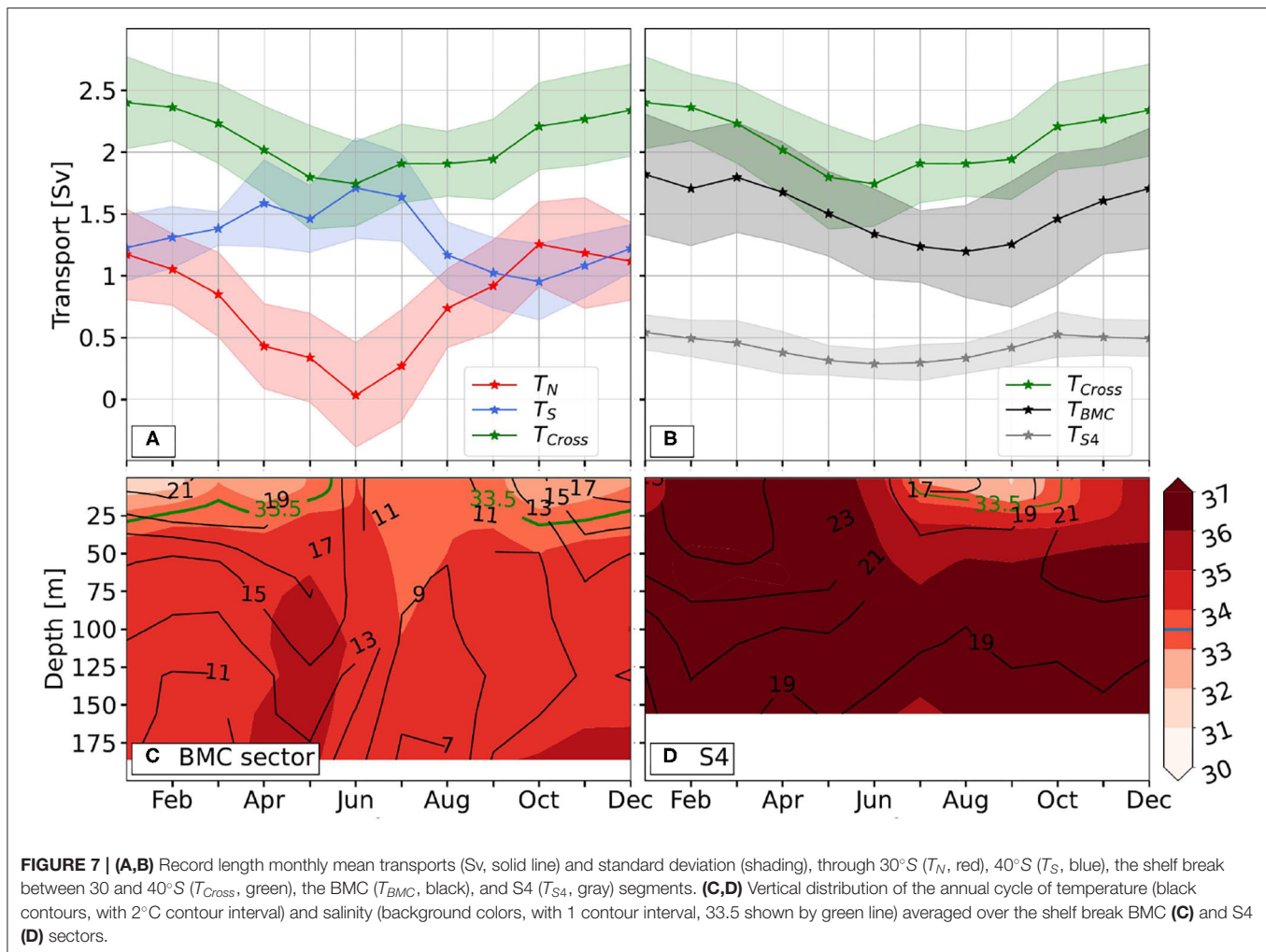
	Interannually	Seasonal	Subannual	Weekly
$T_N$	0.11	0.54	0.82	0.90
$T_S$	0.11	0.32	0.71	0.79
$T_{Cross}$	0.15	0.36	0.72	1.32
$T_{BMC}$	0.20	0.39	0.39	0.43
$T_{S4}$	0.06	0.15	0.19	0.18

Section locations are shown in **Figure 5A**.

**TABLE 3** | Mean transport (Sv) through selected sections for the entire model run (1993–2018), during extreme cross-shore transport events, and during the large transport reversal observed in early May 2015 (see section 4.4).

	Record length (Sv, mean $\pm$ SD)	Positive extreme events $T_{Cross}$ (Sv, mean $\pm$ SD)	Negative extreme events $T_{Cross}$ (Sv, mean $\pm$ SD)	2015-04-29 (Sv)	2015-05-03 (Sv)
$T_N$	$0.78 \pm 1.36$	$2.02 \pm 1.57$	$-2.16 \pm 1.42$	0.80	3.44
$T_S$	$1.31 \pm 1.16$	$4.03 \pm 1.69$	$0.14 \pm 1.28$	-1.82	5.36
$T_{Cross}$	$2.09 \pm 1.60$	$6.05 \pm 0.74$	$-2.02 \pm 0.87$	-1.03	8.80
$T_{BMC}$	$1.53 \pm 0.74$	$2.62 \pm 0.71$	$0.48 \pm 0.64$	0.99	3.11
$T_{S4}$	$0.42 \pm 0.31$	$0.74 \pm 0.34$	$-0.08 \pm 0.25$	0.31	1.10

Section locations are shown in **Figure 5A**.



$T_{Cross}$  is positively correlated with  $T_N$  and  $T_S$ , with  $R^2 = 0.40^*$  and  $0.51^*$ , respectively (**Supplementary Figure 3**). Therefore,  $T_S$  has more control of  $T_{Cross}$  than  $T_N$  at this time scale in agreement with Combes and Matano (2018). The BMC location and  $T_{Cross}$  are not significantly correlated. To better understand the interannual variability of  $T_{Cross}$ , the  $T_S$  and  $T_N$  variability are further explored. To study the possible impact of the variability of the WBCs (Brazil and Malvinas currents), as suggested by numerical simulations (e.g., Matano et al., 2010), we compute the correlation between  $T_S$  and the intensity of the MC ( $I_{MC}$ ) and between  $T_N$  and the intensity of the BC ( $I_{BC}$ ). Another likely driver of  $T_{Cross}$  is the local alongshore wind defined as the wind stress vector at the boundary sections projected on the alongshore direction (38° from true North for both transects following the coastline). Local alongshore wind stress over the northern and southern sections was analyzed with southwesterly wind stress defined as positive. In the southern boundary, positive correlations at the interannual scale are observed between  $T_S$  and  $I_{MC}$ , with  $R^2 = 0.34^*$  (**Supplementary Figure 3B**) and  $T_S$  and alongshore wind stress with  $R^2 = 0.27$  (not significant, **Supplementary Figure 3C**). At the northern boundary,  $T_N$  does

not show a significant correlation with  $I_{BC}$  and alongshore wind stress.

At the seasonal scale,  $T_{Cross}$  variability presents a high positive correlation with  $T_N$  ( $R^2 = 0.77^*$ ) and a negative correlation with  $T_S$  ( $R^2 = 0.22^*$ ; **Figure 8A**). Thus, although the record-length mean  $T_{Cross}$  is mostly contributed by  $T_S$ , the variability at the seasonal scale is driven by variations in  $T_N$ . The BMC location and  $T_{Cross}$  are not correlated. These results are in agreement with Combes and Matano (2018). As the variability of the offshore transport is set by the variability of  $T_N$  and  $T_S$ , it is useful to further analyze the processes that determine the variations of the alongshore transports. The WBCs intensity was analyzed finding a low positive correlation between  $I_{BC}$  and  $T_N$  with  $R^2 = 0.15^*$  and no correlation between  $I_{MC}$  and  $T_S$  (**Figure 8D**).  $T_N$  presents a strong and negative correlation with the alongshore wind stress ( $R^2 = 0.88^*$ , **Figure 8G**) in agreement with Combes et al. (2021). Therefore, high positive (southward)  $T_N$  is associated with northeasterly wind stress that sets up a negative SLA along the coast over the northern transect. The resulting cross-shore pressure gradient leads to a southwestward geostrophic flow through 30°S. Likewise,  $T_S$

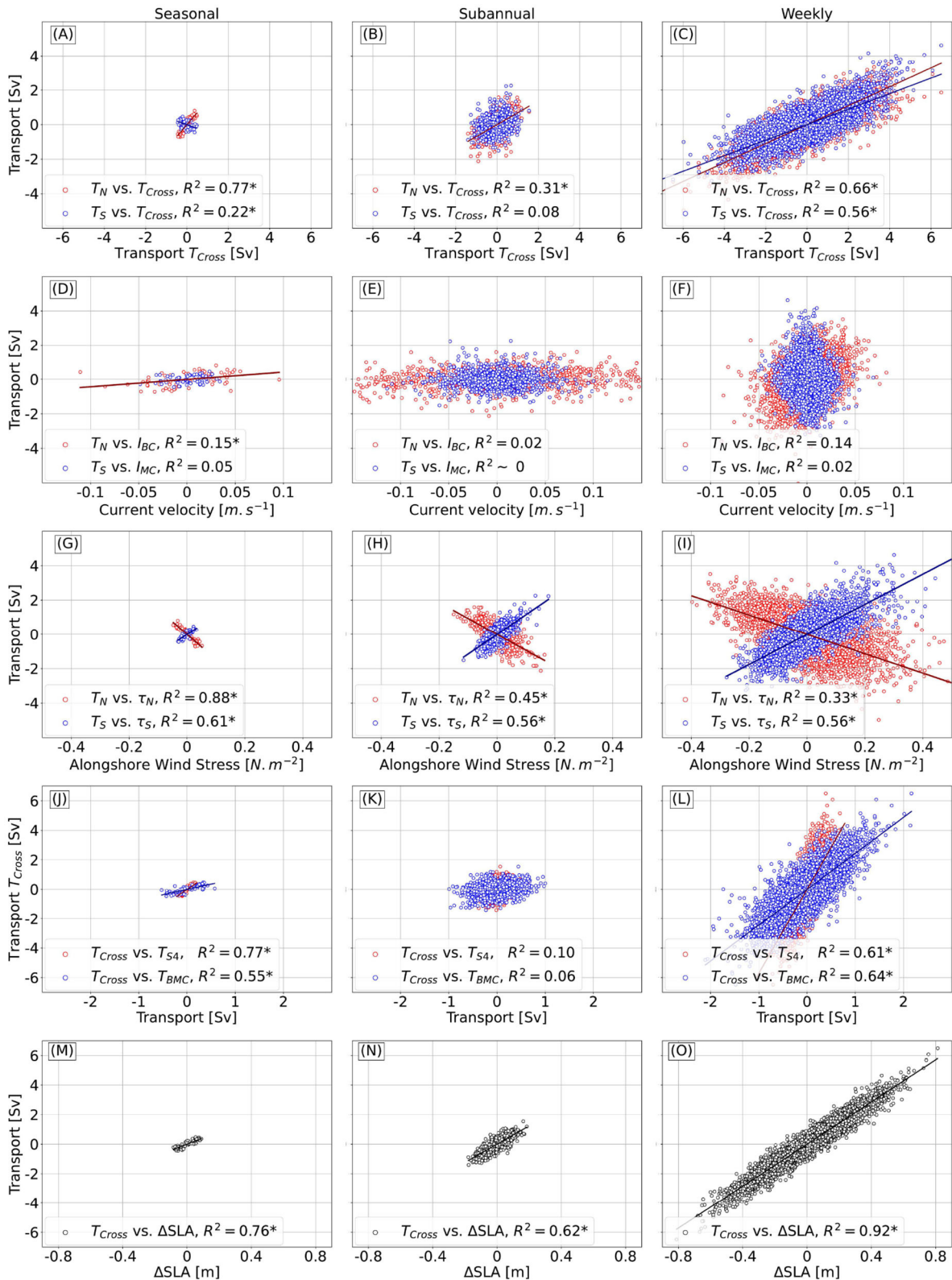


**FIGURE 8 |** (A–C)  $T_N$  (red) and  $T_S$  (blue) vs.  $T_{Cross}$ . (D–F)  $T_N$  vs.  $I_{BC}$  (red) and  $T_S$  vs.  $I_{MC}$  (blue). (G–I)  $T_N$  vs. alongshore wind stress at 30°S (red) and  $T_S$  vs. alongshore wind stress at 40°S (blue). (J–L)  $T_{Cross}$  vs.  $T_{S4}$  (red) and  $T_{BMC}$  (blue). (M–O)  $T_{Cross}$  vs. the difference of inner shelf SLA between 40 and 30°S. (A,D,G,J,M) Seasonal scale, (B,E,H,K,N) subannual scale and (C,F,I,L,O) weekly scale.

presents a positive correlation with the alongshore wind stress ( $R^2 = 0.61^*$ , **Figure 8G**). Therefore, high  $T_S$  are associated with southwesterly wind stress that generates a positive SLA along the coast over the southern transect. The resulting cross-shore pressure gradient is related to a northeastward geostrophic flow through  $40^\circ\text{S}$ . The subtraction of the inner shelf SLA between the southern and northern boundaries represents 76% of the seasonal  $T_{Cross}$  variability (**Figure 8M**). In summary, the inner-shelf SLA variability at the boundaries ( $40$  and  $30^\circ\text{S}$ ) is a good indicator of the  $T_{Cross}$  variability at seasonal time scales.

### 3.2.2. High-Frequency Variability (Subannual and Weekly)

At the subannual scale, the variability of  $T_N$ ,  $T_S$ , and  $T_{Cross}$  is larger than at low frequencies, with standard deviations of 0.82, 0.71, and 0.72 Sv, respectively (**Table 2**). The power spectra of transport variations show substantial energy (38.5, 40.4, and 22.5%, respectively) over a wide range of frequencies (**Figure 6D**).  $T_{S4}$  and  $T_{BMC}$  are very weakly correlated with the transport variations at the northern and southern boundaries ( $R^2 < 0.15$ , **Figure 8K**).

At the weekly time scale, the standard deviations of  $T_N$ ,  $T_S$ , and  $T_{Cross}$  increase to 0.90, 0.79, and 1.32 Sv, respectively (**Table 2**). The power spectra of the transport variability at the weekly time scale present high energy (47.0, 51.6, and 71.9%, respectively) over the entire frequency range ( $<10$  days, **Figure 6D**). The transports through the preferential export routes are clearly related to the intensity of  $T_{Cross}$  with  $R^2 = 0.61^*$  and  $0.64^*$  through the S4 and BMC sectors, respectively (**Figure 8L**). The  $T_{S4}$  variability is more closely associated with the  $T_N$  variability ( $R^2 = 0.71^*$ , not shown) than to  $T_S$  ( $R^2 = 0.25^*$ , not shown), while the  $T_{BMC}$  variability is more closely associated with  $T_S$  variability ( $R^2 = 0.58^*$ , not shown) than to  $T_N$  ( $R^2 = 0.11$ , not shown).

#### 3.2.2.1. Drivers of High-Frequency (Subannual and Weekly) Cross-Shore Transport Variability

Following the analysis of the low-frequency variability, the possible physical mechanisms modulating the high frequencies variability of  $T_{Cross}$  are analyzed. We investigate the possible relationship between the high-frequency variability of  $T_{Cross}$  and the location of the BMC, the shelf and WBCs transports, and the wind stress patterns. At the subannual scale, there is no significant correlation between  $T_{Cross}$  and  $T_S$  (**Figure 8B**) or with the location of the BMC (not shown). In contrast,  $T_{Cross}$  is primarily controlled by  $T_N$  ( $R^2 = 0.31^*$ , **Figure 8B**).  $T_N$  and  $T_S$  are driven by the local alongshore wind stress ( $R^2 = 0.45^*$  and  $0.56^*$ , **Figure 8H**) and not by the WBCs (**Figure 8E**). As pointed out earlier, since local alongshore wind stress sets up SLA variations over the coast and similar to our findings at the seasonal time scale, the inner shelf SLA variations at the northern and southern boundaries are a good indicator of the  $T_{Cross}$  at subannual time scales. Changes in the inner shelf SLA difference at the southern and northern boundaries represent 62% of the  $T_{Cross}$  variability at subannual time scales (**Figure 8N**).

Numerical analyses indicate that although the location of the BMC does not modulate the magnitude of the export of shelf

waters between  $30$  and  $40^\circ\text{S}$ , it does determine the position over the shelf break where the largest offshore transport occurs (Combes and Matano, 2018). Satellite and *in-situ* observations suggest that mesoscale eddies can induce the export of shelf waters (e.g., Guerrero et al., 2014; Manta et al., 2022). As these features have a typical time scale of 10–200 days, they could modulate the  $T_{BMC}$  at the subannual scale. The role of eddies in the cross-shore transports is further suggested by the significant decrease in correlation between the cross-shore ( $T_{Cross}$ ) and the alongshore transports ( $T_N$  and  $T_S$ ) at the subannual time scale (compare **Figures 8A–C**), and between  $T_{Cross}$  and the transport across the BMC sector (**Figure 8K**).

At the weekly time scale, there is no significant correlation between  $T_{Cross}$  and the BMC location (not shown). In contrast,  $T_{Cross}$  is closely associated with  $T_N$  and  $T_S$  ( $R^2 = 0.66^*$  and  $0.56^*$ , respectively, **Figure 8C**). These alongshore transports are modulated by local alongshore wind stress over the northern and southern boundaries ( $R^2 = 0.33^*$  and  $0.56^*$ , respectively, **Figure 8I**) and not by the intensity of WBCs (**Figure 8F**). These transport fluctuations are associated with the inner shelf SLA at  $30$  and  $40^\circ\text{S}$ . Similar to our findings at the seasonal and subannual time scales, the difference between inner shelf SLA at the southern and northern boundaries is a good proxy of  $T_{Cross}$  variability, representing 92% of the weekly variability (**Figure 8O**). These results are in agreement with Lago et al. (2021) who show that the alongshore transport can be estimated based on the difference in SLA between the coast and the shelf. Wind-forced coastal-trapped waves are an additional source of SLA variability at the weekly time scale (Brink, 1991; de Freitas et al., 2021). However, the details of the dynamics of processes leading to the model variability are deferred to a future study.

### 3.3. Analysis of Extreme Transport Events

In this section, the extreme cross-shore transport events are studied based on the daily, unfiltered  $T_N$ ,  $T_S$ , and  $T_{Cross}$ . The monthly distribution of the number of positive extreme events is shown in **Figure 9A**. Recall positive transports imply northward flow over the shelf through  $40^\circ\text{S}$  ( $T_S$ ), southward flow through  $30^\circ\text{S}$  ( $T_N$ ), and offshore flow through the outer shelf between  $30$  and  $40^\circ\text{S}$  ( $T_{Cross}$ ). Extreme southward (positive)  $T_N$  events (red bars in **Figure 9A**) occur more frequently in spring, last  $<3$  days, and reach 6.32 Sv, eight-fold the mean value (0.78 Sv; **Table 4**). Extreme northward (positive)  $T_S$  events (blue bars in **Figure 9A**) are more frequent in austral winter (June–July) and infrequent in summer. Typically, the extreme transport events across the southern boundary last  $<4$  days and reach transports of up to 8.36 Sv (**Table 4**), six-fold the mean value (1.31 Sv). The occurrence of positive  $T_{Cross}$  extreme events (green bars in **Figure 9A**) has two maxima, in fall and spring, and are less frequent in summer. The extreme export events have a shorter duration ( $<2$  days) and present a maximum export transport of 9.45 Sv (more than four-fold the mean export transport, 2.09 Sv). During the entire period, the offshore transports across the BMC sector and S4 account for 73 and 20% of the total transport across the 200 m isobath between  $30$  and  $40^\circ\text{S}$ , respectively. However, during the extreme events, the transports across BMC and S4 decrease to 43 and 12% of the record-mean  $T_{Cross}$ . Therefore, the

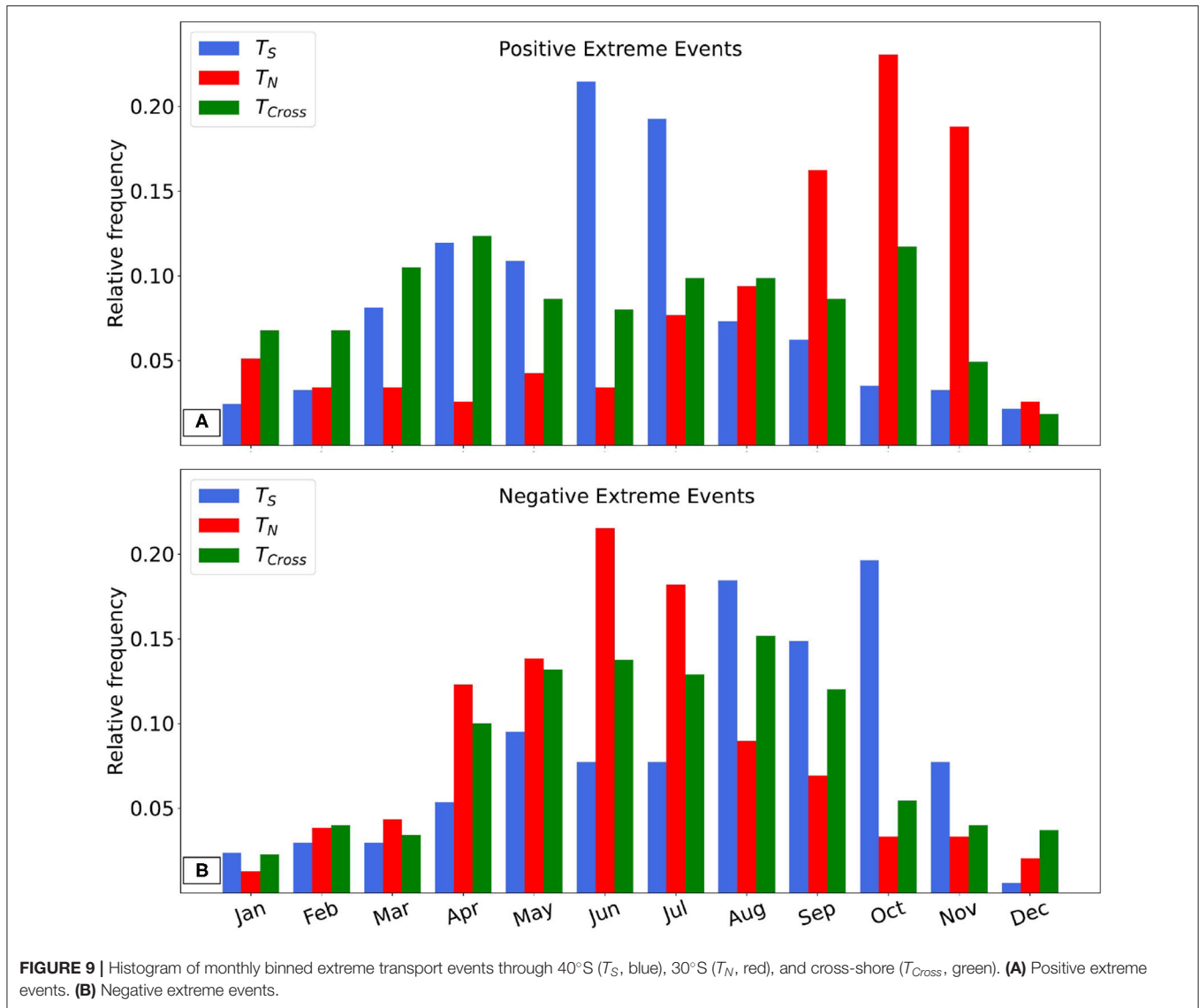


**FIGURE 9** | Histogram of monthly binned extreme transport events through 40°S ( $T_S$ , blue), 30°S ( $T_N$ , red), and cross-shore ( $T_{Cross}$ , green). **(A)** Positive extreme events. **(B)** Negative extreme events.

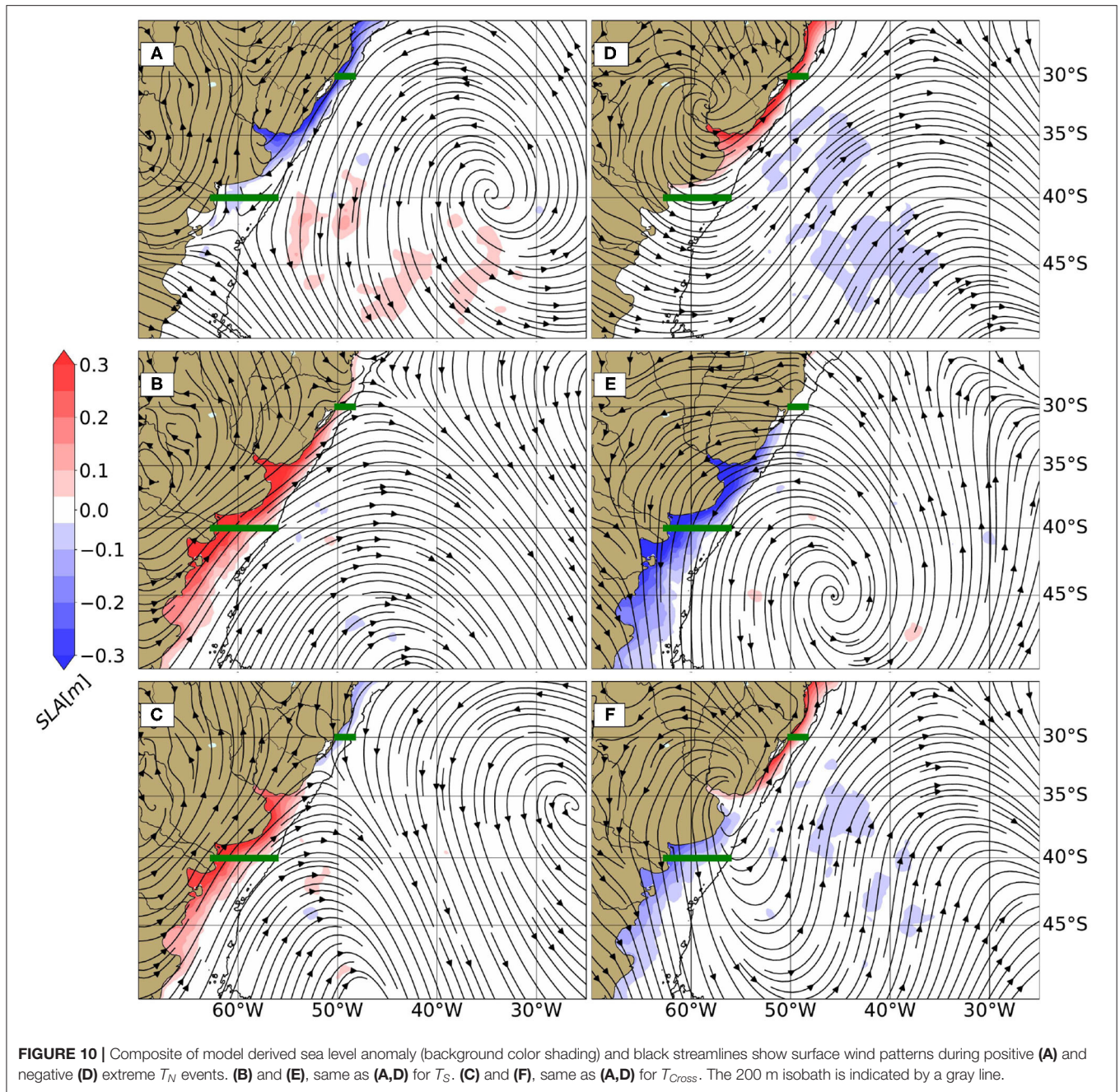
**TABLE 4** | Statistics of extreme transport events through selected sections.

	30°S	40°S	Shelf break
Number of positive events	81 (1.2%)	262 (3.8%)	142 (1.7%)
Duration [min/max][days]	1/3	1/4	1/2
Transport [min/max][Sv]	3.51/6.32	3.63/8.36	5.31/9.45
Number of negative events	246 (4.1%)	129 (1.7%)	255 (3.6%)
Duration [min/max][days]	1/6	1/3	1/4
Transport [min/max][Sv]	-6.54/-1.94	-4.92/-1.00	-6.53/-1.11

Number of extreme events (days) and percent (relative to the total number of model days). Transports in Sv.

offshore transport during the extreme export events is spatially more uniformly distributed. During the average positive  $T_{Cross}$  export event ( $T_{Cross}$  mean of 6.08 Sv), 4.27% of the total volume of shelf waters between 30 and 40°S is exported to the open ocean.

The monthly distribution of the number of negative extreme events is shown in **Figure 9B**. Negative (northward) extreme  $T_N$  events are more frequent in June–July and uncommon in summer, last <6 days, and reach  $-6.54$  Sv. Negative (southward) extreme  $T_S$  events occur more frequently between August and October and infrequently in summer, last <3 days, and reach transports of up to  $-4.92$  Sv. The occurrence of negative extreme  $T_{Cross}$  events is maximum during winter and minimum during summer. The extreme cross-shore transport events have a short duration (between 1 and 4 days) and the maximum onshore transport reaches  $-6.53$  Sv. During these negative cross-shore transport events the BMC sector continues to be an export location with offshore transports of shelf waters of  $0.48 \pm 0.64$  Sv (**Table 3**). Therefore, the on-shelf intrusion of open ocean water is distributed over the remaining of the shelf break domain (**Figure 5B**), including S4. These negative extreme events represent on average 1.79% of the total shelf volume between 30 and 40°S.



The extreme events have a typical duration in the weekly time scale. As discussed in section 3.2.2.1, the variability on this scale is mostly driven by the local alongshore wind stress. Therefore, it is useful to further explore the possible association between variations in regional wind patterns and extreme transport events. Recall that southwesterly wind stress is referred to as positive and northeasterly wind stress as negative. A composite (average fields during extreme events) of positive  $T_N$  extreme events is characterized by negative (northeasterly) local alongshore wind stress ( $\sim -0.27 \text{ N.m}^{-2}$ ) at  $30^\circ\text{S}$  associated with a high atmospheric pressure center located near  $40^\circ\text{S}$ – $35^\circ\text{W}$

(Figure 10A). Consequently, a negative SLA develops along the coast, which is most intense north of the RDP estuary. The resulting cross-shore pressure gradient leads to a southwestward geostrophic flow north of  $38^\circ\text{S}$ . The negative SLA and the associated geostrophic flow weaken near the southern boundary. The negative  $T_N$  extreme events are characterized by positive local alongshore wind stress ( $\sim 0.16 \text{ N.m}^{-2}$ ) at  $30^\circ\text{S}$ , associated with a high atmosphere pressure center located near  $32.5^\circ\text{S}$ – $59.5^\circ\text{W}$  (Figure 10D). Consequently, a positive SLA develops along the coast north of  $38^\circ\text{S}$ , which leads to a northeastward geostrophic flow at  $30^\circ\text{S}$ .

The positive extreme events in  $T_S$  are associated with positive (southwesterly) local alongshore wind stress ( $\sim 0.21 \text{ N.m}^{-2}$ ) at  $40^\circ\text{S}$ , associated with a low atmospheric pressure center located south of  $50^\circ\text{S}$  (Figure 10B), that generates southwesterly wind stress over the continental shelf south of  $30^\circ\text{S}$ . This intense wind stress creates a positive SLA along the coast in the entire domain, which leads to a relatively strong northeastward geostrophic flow at  $40^\circ\text{S}$ . This northeastward flow extends northeastward, also leading to northeastward (negative) flow across the northern boundary. Conversely, negative  $T_S$  extreme events are associated with negative (northeasterly) local alongshore wind stress at  $40^\circ\text{S}$  ( $\sim -0.13 \text{ N.m}^{-2}$ ) associated with a high atmospheric pressure center located at  $45^\circ\text{S}$ – $47.5^\circ\text{W}$  (Figure 10E). In response to this wind stress pattern, there is a negative inner shelf SLA south of  $30^\circ\text{S}$  and an associated southwestward flow across the southern boundary (Figure 10E).

The positive  $T_{Cross}$  extreme events are characterized by southwesterly wind stress at  $40^\circ\text{S}$  ( $\sim 0.22 \text{ N.m}^{-2}$ ) and northeasterly wind stress at  $30^\circ\text{S}$  ( $\sim -0.08 \text{ N.m}^{-2}$ ). A low atmospheric pressure center located near  $50^\circ\text{S}$ – $50^\circ\text{W}$  (Figure 10C) generates southwesterly wind stress over the continental shelf south of  $40^\circ\text{S}$  and a positive SLA along the coast south of  $34^\circ$ . Thus, this atmospheric circulation pattern leads to relatively intense northeastward transport ( $4.03 \pm 1.69 \text{ Sv}$ , Table 3) over the shelf across the southern boundary ( $T_S$ ,  $40^\circ\text{S}$ ). Conversely, a high atmospheric pressure center located near  $35^\circ\text{S}$ – $28^\circ\text{W}$  generates northeasterly wind stress over the continental shelf north of  $30^\circ\text{S}$ . In response to this wind stress pattern, a weak negative SLA develops in the inner shelf north of  $33^\circ\text{S}$ , this negative anomaly leads to southwestward transport ( $2.02 \pm 1.57 \text{ Sv}$ , Table 3) over the shelf across the northern boundary ( $T_N$ ,  $30^\circ\text{S}$ ). The resulting mass convergence over the shelf between  $30$  and  $40^\circ\text{S}$  is compensated by a strong offshore flow of shelf waters. The negative extreme events of  $T_{Cross}$  are associated with a high atmospheric pressure center located over the RDP (Figure 10F). This feature leads to northwesterly wind stress at  $40^\circ\text{S}$  ( $\sim -0.04 \text{ N.m}^{-2}$ ) that generates a negative SLA over the coast south of the RDP and southwesterly wind stress at  $30^\circ\text{S}$  ( $\sim 0.14 \text{ N.m}^{-2}$ ) that generates a positive SLA north of RDP. As a result, a weakening of northeastward flow across the southern boundary ( $T_S$ ,  $0.14 \pm 1.28 \text{ Sv}$ ) and a northeastward transport across the northern boundary are observed ( $T_N$ ,  $-2.16 \pm 1.42 \text{ Sv}$ ). Analogous to the positive extreme events, the mass divergence over the shelf between  $30$  and  $40^\circ\text{S}$  is compensated by an influx of deep-ocean waters to the shelf. These import events can have an important biogeochemical impact on the shelf.

Intense Malvinas Current intrusions over the shelf, causing substantial cooling, increased salinity, and elevated surface chlorophyll concentrations have been reported near  $41^\circ\text{S}$  (Piola et al., 2010). A recent analysis of *in-situ* observations collected in late April 2016 between  $34$  and  $38^\circ\text{S}$  presents relatively cold, salty, and high-nutrient waters in the outer shelf near  $36.5^\circ\text{S}$  (Manta et al., 2022, their Figures 2C,F, 5C). These observations suggest onshore flow of subantarctic water from the Malvinas Current. Our model analysis indicates that  $T_{Cross}$  reached  $-2.55 \text{ Sv}$  in the previous days. About 30% of this inflow occurred across the BMC ( $T_{BMC} \sim -0.81 \text{ Sv}$ ). As might be expected, on average  $T_{BMC}$  is positive and peaks in the BMC sector

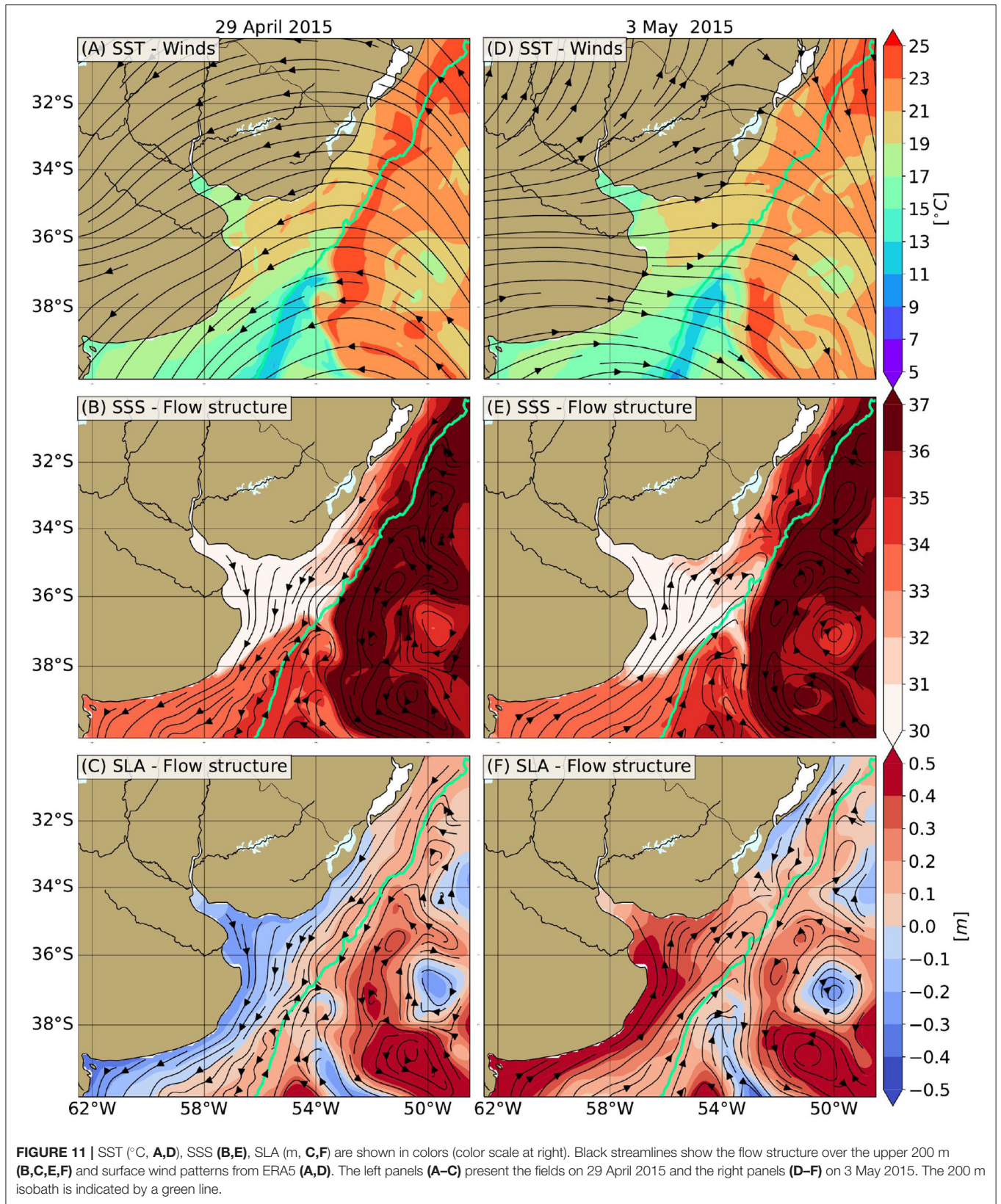
of the shelf-break (Supplementary Figure 4). However, there are a few instances (about 2.20% of the time) when  $T_{BMC}$  is negative (onshore), as observed in late April 2016. In the model, the relatively intense import of slope waters was associated with northeastward flows of  $-4.09 \text{ Sv}$  across  $30^\circ\text{S}$  and  $1.54 \text{ Sv}$  across  $40^\circ\text{S}$ , which peaked on 27 April 2016. Thus, the model circulation is consistent with the observation of subantarctic waters in the outer shelf south of the BMC reported by Manta et al. (2022). Moreover, the model results suggest that the onshelf flow observed in late April 2016 between  $30$  and  $40^\circ$  was a response to divergence of the along-shore circulation, which was mostly driven by the pattern of alongshore winds. However, in agreement with the observations of Manta et al. (2022), mesoscale eddies that approach the outer shelf may create a fine scale structure of relatively intense cross-shore flows (see Supplementary Figure 5). In addition, highly non-linear submesoscale features of characteristic scale  $<10 \text{ km}$ , not resolved by the GLORYS reanalysis, are ubiquitous in the Brazil/Malvinas Confluence (Orúe-Echevarría et al., 2019), and may further contribute to cross-shelf exchanges.

### 3.3.1. The $T_{Cross}$ Event of Early May 2015

From 29 April to 3 May 2015 the model produces large transport anomalies across  $40^\circ\text{S}$ . This event is of interest because it was also clearly detected by direct current observations close to  $40^\circ\text{S}$  (see section 3.1.3 and Lago et al., 2019, 2021). On 29 April 2015, the circulation is characteristic of an extreme negative  $T_S$  event, with northeasterly wind stress (Figure 11A) generating a negative inner shelf SLA associated with southwestward flow over the shelf south of  $33^\circ\text{S}$  (Figure 11C). At that time the flow over much of the shelf is southward, reaching  $-1.82 \text{ Sv}$  across  $40^\circ\text{S}$  and  $+0.8 \text{ Sv}$  across  $30^\circ\text{S}$ . Recall that we have defined southward flow at  $30^\circ\text{S}$  as positive. In response to the divergence of the alongshore circulation,  $T_{Cross}$  presents a negative (onshore) transport ( $-1.03 \text{ Sv}$ ) (Table 3). The flow structure indicates intrusions of slope waters: relatively cold-salty waters from the MC south of  $37^\circ\text{S}$  and warm-salty waters from the BC near  $31^\circ\text{S}$  (Figure 11B). On 3 May, the circulation has evolved to one that is characteristic of extreme offshore transport events with  $T_{Cross}$  reaching  $8.80 \text{ Sv}$  (Table 3). This very large export of relatively fresh shelf waters (Figure 11E) is mediated by strong convergence of the alongshore circulation over the shelf (Figure 11F). At that time the flow across  $40^\circ\text{S}$  reverses to northward, with  $T_S$  reaching  $5.36 \text{ Sv}$  in response to a positive SLA over the inner shelf generated by local southwesterly/westerly wind stress (Figure 11D). In contrast, the flow at  $30^\circ\text{S}$  is still southwestward (positive), with  $T_N$  reaching  $3.44 \text{ Sv}$ , in response to a negative SLA over the inner shelf which in turn results from local northeasterly wind stress at that location. Shelf water export during extreme events does not necessarily follow the most frequently observed pathways across the BMC and S4 segments, it occurs across most of the shelf break, with a maximum export occurring between  $32$  and  $36.5^\circ\text{S}$ .

## 4. SUMMARY AND CONCLUSIONS

The variability and drivers of the cross-shelf exchanges between the Southwestern Atlantic shelf between  $30$  and  $40^\circ\text{S}$  and the open ocean have been analyzed using a high-resolution





ocean reanalysis. Independent hydrographic data from 12 oceanographic surveys carried out on the shelf near 34°S between 2003 and 2018, 24 years of gridded altimetry data (note that GLORYS12V1 assimilates along-track altimetry), and an independent estimate of alongshore transport near 39°S based on mooring data were used to evaluate the model performance. There is a substantial agreement near 39°S between daily alongshore shelf transports from observations and the model. The model also shows similar patterns of SLA variability to the altimetry derived data, although with somewhat larger differences over the Río de la Plata. The relatively low spatial and temporal resolution of the gridded altimetric product does not allow the representation of mesoscale, high-frequency processes (3–10 day periods) which are generated by the model's internal dynamics. In addition, the model presents an overall good agreement with geostrophic velocities calculated from the hydrographic data over the shelf near 34°S.

Once the reanalysis performance was assessed, we analyzed the cross-shore transport and its temporal and spatial variability. The record length mean cross-shore transport [mean  $\pm$  standard deviation] between 30 and 40°S ( $T_{Cross}$ ) is  $2.09 \pm 1.60$  Sv, with positive transport representing offshore flow. Sixty-three percent of the mean  $T_{Cross}$  was contributed by northward transport across 40°S ( $T_S$ ) and the remaining 37% by southward transport across 30°S ( $T_N$ ). Most of the offshore flow (73%) occurs in the vicinity of the BMC and about 20% in the vicinity of 32°S.  $T_{Cross}$  presents more variability at high frequencies, 71.9 and 22.5% of energy in the weekly and subannual scales, respectively than at low frequencies, 4.9 and 0.7% of energy in the seasonal and interannual scales, respectively.

At the interannual scale, the cross-shore transport variability ( $T_{Cross}$ ) is more controlled by the alongshore transport over the shelf across 40°S ( $T_S$ , 51%) than across 30°S ( $T_N$ , 40%) and  $T_S$  is moderately modulated by the intensity of the Malvinas Current. At the annual scale, there is high spectral energy in all transports. In the mean,  $T_N$  and  $T_S$  are positive throughout the year.  $T_N$  presents a maximum (southwestward) transport in October and a minimum from April to July while  $T_S$  has the opposite behavior, though with somewhat weaker amplitude. Consequently,  $T_{Cross}$  is positive (offshore) throughout the year, and presents a maximum in January and a minimum in June. The alongshore transports over the shelf are driven by local alongshore wind stress.  $T_{Cross}$  variability is mostly driven by  $T_N$  variability. At the subannual scale,  $T_N$  and  $T_S$  are driven by the local alongshore wind stress and  $T_{Cross}$ , particularly near 32°S, is primarily controlled by  $T_N$ . At the weekly time scale, both  $T_N$  and  $T_S$  are also strongly modulated by the local alongshore wind stress.  $T_S$  has control over the export of shelf waters across the BMC, while  $T_N$  is more closely associated with cross-shore fluxes at 32°S.

Extreme alongshore transport events across 30 and 40°S have been analyzed using the model's daily output. These events are closely associated with local wind stress with a duration of <6 and 4 days, respectively. During positive events, defined as convergence of alongshore flow over the shelf, transports reach 6 and 8 times their long-term averages, respectively. Extreme offshore transport events reach up to 9.45 Sv. These high export events last <2 days and are more frequent during fall and spring.

Despite the short duration of intense export events, 4.3% of the total volume of shelf water between 30 and 40°S is exported to the adjacent deep ocean during the average event (6.05 Sv). These large exports of shelf waters must lead to freshening of upper ocean waters as revealed by *in-situ* and satellite observations. In contrast, negative extreme events drive open ocean water intrusions of up to 6.53 Sv. These onshore flow events last <4 days and are more frequent in winter. During the average onshore flow event, 1.8% of the total volume of shelf water is replaced by slope water. The inflows of open ocean waters, particularly those of salty subtropical waters from the Brazil Current, must cause a substantial salinification of outer shelf waters and those from the Malvinas Currents contribute with nutrients.

Alongshore winds over the shelf generate SLAs over the inner shelf. The associated cross-shore pressure gradient leads to alongshore geostrophic flows. Southwesterly winds over the southern boundary (40°S) drive a positive SLA on the inner shelf and northeasterly winds over the northern boundary (30°S) generate a negative SLA on the inner shelf. The resulting cross-shore pressure gradients drive convergent alongshore geostrophic flows over the shelf and export of shelf waters to the open ocean. Conversely, opposite winds generate divergent alongshore geostrophic flows over the shelf and drive the import of slope water to the shelf. These SLA variations on the inner shelf, mostly controlled by alongshore wind variations, exert an important control on alongshore circulation, and cross-shelf exchange, on seasonal, subannual, and weekly scales and also on the extreme events.

## DATA AVAILABILITY STATEMENT

Publicly available datasets were analyzed in this study. These data can be found at: GLORYS12V1 ocean reanalysis (<https://resources.marine.copernicus.eu/documents/QUID/CMEMS-GLO-QUID-001-030.pdf>); ERA5 atmospheric reanalysis (<https://www.ecmwf.int/en/forecasts/datasets/reanalysis-data-sets/era5>); and altimetry data from Copernicus Marine [https://resources.marine.copernicus.eu/product-detail/SEALEVEL\\_GLO\\_PHY\\_L4\\_MY\\_008\\_047/INFORMATION](https://resources.marine.copernicus.eu/product-detail/SEALEVEL_GLO_PHY_L4_MY_008_047/INFORMATION)). *In situ* data located near 39° used to evaluate the model performance can be found in public SE-ANOE public data repository at: <https://www.seano.org/data/00403/51492/> and <https://www.seano.org/recordview>. Hydrographic data near 34° used to evaluate the model performance can be found in public data repository at [ftp://ftp.aoml.noaa.gov/phod/pub/SAM/hydrographic\\_data/](ftp://ftp.aoml.noaa.gov/phod/pub/SAM/hydrographic_data/), in this in-text data citation references: Charo et al. (2020).

## AUTHOR CONTRIBUTIONS

GB processed the hydrographic and the model data and did the model performance evaluation and the transport calculations and prepared the manuscript with contributions from all co-authors. All authors participated in the scientific interpretation of the results. All authors contributed to the article and approved the submitted version.

## FUNDING

This work was partially funded by the Inter-American Institute for Global Change Research (IAI) grants CRN3070 (US National Science Foundation grant GEO-1128040) and SGP-HW 017. Additional funding was provided by IAI/CONICET grant RD3347, FONCYT grant PICT2016-0557, and SECYT-UNS grant 24-F079.

## ACKNOWLEDGMENTS

GB was supported by a doctoral fellowship from Consejo Nacional de Investigaciones Científicas y Técnicas (Argentina). The hydrographic data were collected as part of the South

Atlantic Meridional Overturning Circulation initiative ([https://www.aoml.noaa.gov/phod/SAMOC\\_international/](https://www.aoml.noaa.gov/phod/SAMOC_international/)). We thank the science parties and crews of the NICOP/Plata, SAM, and STSF cruises that collected the data in the Albardão transect. We particularly thank Marcela Charo (SHN, Argentina) for data calibration and processing and Loreley Lago (CIMA, Argentina) for providing the observational transport time series shown in **Figure 4**.

## SUPPLEMENTARY MATERIAL

The Supplementary Material for this article can be found online at: <https://www.frontiersin.org/articles/10.3389/fmars.2022.855183/full#supplementary-material>

## REFERENCES

- Ballarotta, M., Ubelmann, C., Pujol, M.-I., Taburet, G., Fournier, F., Legeais, J.-F., et al. (2019). On the resolutions of ocean altimetry maps. *Ocean Sci.* 15, 1091–1109. doi: 10.5194/os-15-1091-2019
- Berden, G., Charo, M., Möller O. O. Jr, and Piola, A. R. (2020). Circulation and hydrography in the western south Atlantic shelf and export to the deep adjacent ocean: 30°S to 40°S. *J. Geophys. Res.* 125, e2020JC016500. doi: 10.1029/2020JC016500
- Bordin, L. H., Machado, E. d. C., Carvalho, M., Freire, A. S., and Fonseca, A. L. (2019). Nutrient and carbon dynamics under the water mass seasonality on the continental shelf at the South Brazil Bight. *J. Mar. Syst.* 189, 22–35. doi: 10.1016/j.jmarsys.2018.09.006
- Borús, J., Uriburu Quirno, M., and Calvo, D. (2017). *Evaluación de Caudales Mensuales Descargados por los Grandes ríos del Sistema del Plata al Estuario del Río de la Plata*. Ezeiza: Alerta Hidrológico-Instituto Nacional del Agua y el Ambiente.
- Braga, E. S., Chiozzini, V. C., Berbel, G. B., Maluf, J. C., Aguiar, V. M., Charo, M., et al. (2008). Nutrient distributions over the Southwestern South Atlantic continental shelf from Mar del Plata (Argentina) to Itajaí (Brazil): winter-summer aspects. *Contin. Shelf Res.* 28, 1649–1661. doi: 10.1016/j.csr.2007.06.018
- Brink, K. (1991). Coastal-trapped waves and wind-driven currents over the continental shelf. *Annu. Rev. Fluid Mech.* 23, 389–412. doi: 10.1146/annurev.fl.23.010191.002133
- Cabanes, C., Grouazel, A., von Schuckmann, K., Hamon, M., Turpin, V., Coatanoan, C., et al. (2013). The CORA dataset: validation and diagnostics of *in-situ* ocean temperature and salinity measurements. *Ocean Sci.* 9, 1–18. doi: 10.5194/os-9-1-2013
- Charo, M., Guerrero, R., and Piola, A. (2020). *Subtropical Shelf Front cruise-Conductivity-Temperature-Depth (CTD) Data*. Harvard Dataverse.
- Chen, C.-T. A., Liu, K.-K., and Macdonald, R. (2003). “Continental margin exchanges,” in *Ocean Biogeochemistry*, Fasham MJR, editor (Berlin: Springer), 53–97. doi: 10.1007/978-3-642-55844-3\_4
- Chidichimo, M., Piola, A., Meinen, C., Perez, R., Campos, E., Dong, S., et al. (2021). Brazil current volume transport variability during 2009–2015 from a long-term moored array at 34.5°S. *J. Geophys. Res.* 126, e2020JC017146. doi: 10.1029/2020JC017146
- Christensen, J. P., Murray, J. W., Devol, A. H., and Codispoti, L. A. (1987). Denitrification in continental shelf sediments has major impact on the oceanic nitrogen budget. *Glob. Biogeochem. Cycles* 1, 97–116. doi: 10.1029/GB001i002p00097
- Ciotti, Á. M., Odebrecht, C., Fillmann, G., and Moller O. O. Jr (1995). Freshwater outflow and Subtropical Convergence influence on phytoplankton biomass on the southern Brazilian continental shelf. *Cont. Shelf Res.* 15, 1737–1756. doi: 10.1016/0278-4343(94)00091-Z
- Combes, V., and Matano, R. P. (2014a). Trends in the Brazil/Malvinas confluence region. *Geophys. Res. Lett.* 41, 8971–8977. doi: 10.1002/2014GL062523
- Combes, V., and Matano, R. P. (2014b). A two-way nested simulation of the oceanic circulation in the southwestern Atlantic. *J. Geophys. Res.* 119, 731–756. doi: 10.1002/2013JC009498
- Combes, V., and Matano, R. P. (2018). The Patagonian shelf circulation: drivers and variability. *Prog. Oceanogr.* 167, 24–43. doi: 10.1016/j.pocean.2018.07.003
- Combes, V., Matano, R. P., and Palma, E. D. (2021). Circulation and cross-shelf exchanges in the northern shelf region of the southwestern Atlantic: kinematics. *J. Geophys. Res.* 126, e2020JC016959. doi: 10.1029/2020JC016959
- de Freitas, P. P., de Moraes Paiva, A., Cirano, M., Mill, G. N., da Costa, V. S., Gabioux, M., et al. (2021). Coastal trapped waves propagation along the southwestern Atlantic continental shelf. *Cont. Shelf Res.* 226, 104496. doi: 10.1016/j.csr.2021.104496
- de Haas, H., van Weering, T. C., and de Stigter, H. (2002). Organic carbon in shelf seas: sinks or sources, processes and products. *Cont. Shelf Res.* 22, 691–717. doi: 10.1016/S0278-4343(01)00093-0
- Franco, B. C., Palma, E. D., Combes, V., Acha, E. M., and Saraceno, M. (2018). Modeling the offshore export of Subantarctic Shelf Waters from the Patagonian shelf. *J. Geophys. Res.* 123, 4491–4502. doi: 10.1029/2018JC013824
- Franco, B. C., Palma, E. D., Combes, V., and Lasta, M. L. (2017). Physical processes controlling passive larval transport at the Patagonian Shelf Break Front. *J. Sea Res.* 124, 17–25. doi: 10.1016/j.seares.2017.04.012
- Gattuso, J.-P., Frankignoulle, M., and Wollast, R. (1998). Carbon and carbonate metabolism in coastal aquatic ecosystems. *Annu. Rev. Ecol. Syst.* 29, 405–434. doi: 10.1146/annurev.ecolsys.29.1.405
- Goni, G. J., and Wainer, I. (2001). Investigation of the Brazil Current front variability from altimeter data. *J. Geophys. Res.* 106, 31117–31128. doi: 10.1029/2000JC000396
- Gordon, A. L., and Greengrove, C. L. (1986). Geostrophic circulation of the Brazil-Falkland confluence. *Deep Sea Res. Part A.Oceanogr.* 33, 573–585. doi: 10.1016/0198-0149(86)90054-3
- Guerrero, R. A., Piola, A. R., Fenco, H., Matano, R. P., Combes, V., Chao, Y., et al. (2014). The salinity signature of the cross-shelf exchanges in the Southwestern Atlantic Ocean: satellite observations. *J. Geophys. Res.* 119, 7794–7810. doi: 10.1002/2014JC010113
- Hersbach, H., Bell, B., Berrisford, P., Hirahara, S., Horányi, A., Mu noz-Sabater, J., et al. (2020). The era5 global reanalysis. *Q. J. R. Meteorol. Soc.* 146, 1999–2049. doi: 10.1002/qj.3803
- Hirsch, J. J., Killworth, P. D., and Blundell, J. R. (2007). Subannual, seasonal, and interannual variability of the North Atlantic meridional overturning circulation. *J. Phys. Oceanogr.* 37, 1246–1265. doi: 10.1175/JPO3049.1
- Lago, L. S., Saraceno, M., Martos, P., Guerrero, R. A., Piola, A. R., Paniagua, G. F., et al. (2019). On the wind contribution to the variability of ocean currents over wide continental shelves: a case study on the northern Argentine continental shelf. *J. Geophys. Res.* 124, 7457–7472. doi: 10.1029/2019JC015105
- Lago, L. S., Saraceno, M., Piola, A. R., and Ruiz-Etcheverry, L. A. (2021). Volume transport variability on the northern Argentine continental shelf from *in situ* and satellite altimetry data. *J. Geophys. Res.* 126, e2020JC016813. doi: 10.1029/2020JC016813

- Lellouche, J.-M., Greiner, E., Le Galloudec, O., Garric, G., Regnier, C., Drevillon, M., et al. (2018). Recent updates to the Copernicus Marine Service global ocean monitoring and forecasting real-time 1/12° high-resolution system. *Ocean Sci.* 14, 1093–1126. doi: 10.5194/os-14-1093-2018
- Lumpkin, R., and Garzoli, S. (2011). Interannual to decadal changes in the western South Atlantic's surface circulation. *J. Geophys. Res.* 116, 1–10. doi: 10.1029/2010JC006285
- Madec, G., Bourdallé-Badie, R., Bouttier, P.-A., Bricaud, C., Bruciaferri, D., Calvert, D., et al. (2017). *Nemo Ocean Engine. Note du Pôle de Modélisation de l'Institut Pierre-Simon Laplace, No. 27*. Institut Pierre-Simon Laplace.
- Malan, N., Archer, M., Roughan, M., Cetina-Heredia, P., Hemming, M., Rocha, C., et al. (2020). Eddy-driven cross-shelf transport in the East Australian Current separation zone. *J. Geophys. Res.* 125, e2019JC015613. doi: 10.1029/2019JC015613
- Manta, G., Speich, S., Barreiro, M., Trinchin, R., De Mello, C., Laxenaire, R., et al. (2022). Shelf water export at the Brazil-malvinas confluence evidenced from combined *in-situ* and satellite observations. *Front. Marine Sci.* doi: 10.3389/fmars.2022.857594. [In Press].
- Matano, R., Palma, E. D., and Piola, A. R. (2010). The influence of the Brazil and Malvinas Currents on the Southwestern Atlantic Shelf circulation. *Ocean Sci.* 6, 983–995. doi: 10.5194/os-6-983-2010
- Matano, R. P., Combes, V., Piola, A. R., Guerrero, R., Palma, E. D., Ted Strub, P., et al. (2014). The salinity signature of the cross-shelf exchanges in the Southwestern Atlantic Ocean: numerical simulations. *J. Geophys. Res.* 119, 7949–7968. doi: 10.1002/2014JC010116
- Möller, O. O. Jr, Piola, A. R., Freitas, A. C., and Campos, E. J. (2008). The effects of river discharge and seasonal winds on the shelf off southeastern South America. *Cont. Shelf Res.* 28, 1607–1624. doi: 10.1016/j.csr.2008.03.012
- Orúe-Echevarría, D., Castellanos, P., Sans, J., Emelianov, M., Vallés-Casanova, I., and Pelegrí, J. L. (2019). Temperature spatiotemporal correlation scales in the Brazil-Malvinas Confluence from high-resolution *in situ* and remote sensing data. *Geophys. Res. Lett.* 46, 13234–13243. doi: 10.1029/2019GL084246
- Palma, E., Matano, R., and Piola, A. (2004). A numerical study of the Southwestern Atlantic Shelf circulation: Barotropic response to tidal and wind forcing. *J. Geophys. Res.* 109, C08014. doi: 10.1029/2004JC002315
- Palma, E. D., and Matano, R. P. (2009). Disentangling the upwelling mechanisms of the south Brazil bight. *Cont. Shelf Res.* 29, 1525–1534. doi: 10.1016/j.csr.2009.04.002
- Piola, A. R., Campos, E. J., Möller, O. O. Jr, Charo, M., and Martinez, C. (2000). Subtropical shelf front off eastern South America. *J. Geophys. Res.* 105, 6565–6578. doi: 10.1029/1999JC000300
- Piola, A. R., Martínez Avellaneda, N., Guerrero, R. A., Jardón, F. P., Palma, E. D., and Romero, S. I. (2010). Malvinas-slope water intrusions on the northern Patagonia continental shelf. *Ocean Sci.* 6, 345–359. doi: 10.5194/os-6-345-2010
- Piola, A. R., Matano, R. P., Palma, E. D., Moller, O. O., and Campos, E. J. D. (2005). The influence of the Plata River discharge on the western South Atlantic shelf. *Geophys. Res. Lett.* 32, 1–4. doi: 10.1029/2004GL021638
- Piola, A. R., Möller, O. O. Jr, Guerrero, R. A., and Campos, E. J. (2008). Variability of the subtropical shelf front off eastern South America: Winter 2003 and summer 2004. *Cont. Shelf Res.* 28, 1639–1648. doi: 10.1016/j.csr.2008.03.013
- Piola, A. R., Palma, E. D., Bianchi, A. A., Castro, B. M., Dottori, M., Guerrero, R. A., et al. (2018). “Physical oceanography of the SW Atlantic Shelf: a review,” in *Plankton Ecology of the Southwestern Atlantic—From the Subtropical to the Subantarctic Realm*, eds M. Hoffmeyer, M. E. Sabatini, F. Brandini, D. Calliari, and N. Santinelli (Cham: Springer), 37–56. doi: 10.1007/978-3-319-77869-3\_2
- Pujol, M.-I., Faugère, Y., Taburet, G., Dupuy, S., Pelloquin, C., Ablain, M., et al. (2016). Duacs DT2014: the new multi-mission altimeter data set reprocessed over 20 years. *Ocean Sci.* 12, 1067–1090. doi: 10.5194/os-12-1067-2016
- Rabouille, C., Mackenzie, F. T., and Ver, L. M. (2001). Influence of the human perturbation on carbon, nitrogen, and oxygen biogeochemical cycles in the global coastal ocean. *Geochim. Cosmochim. Acta* 65, 3615–3641. doi: 10.1016/S0016-7037(01)00760-8
- Reynolds, R. W., Smith, T. M., Liu, C., Chelton, D. B., Casey, K. S., and Schlax, M. G. (2007). Daily high-resolution-blended analyses for sea surface temperature. *J. Clim.* 20, 5473–5496. doi: 10.1175/2007JCLI1824.1
- Roughan, M., Macdonald, H. S., Baird, M. E., and Glasby, T. M. (2011). Modelling coastal connectivity in a Western Boundary Current: Seasonal and inter-annual variability. *Deep Sea Res. Part II Top. Stud. Oceanogr.* 58, 628–644. doi: 10.1016/j.dsr2.2010.06.004
- Strub, P. T., James, C., Combes, V., Matano, R. P., Piola, A. R., Palma, E. D., et al. (2015). Altimeter-derived seasonal circulation on the Southwest Atlantic shelf: 27° – 43° S. *J. Geophys. Res.* 120, 3391–3418. doi: 10.1002/2015JC010769

**Conflict of Interest:** The authors declare that the research was conducted in the absence of any commercial or financial relationships that could be construed as a potential conflict of interest.

**Publisher's Note:** All claims expressed in this article are solely those of the authors and do not necessarily represent those of their affiliated organizations, or those of the publisher, the editors and the reviewers. Any product that may be evaluated in this article, or claim that may be made by its manufacturer, is not guaranteed or endorsed by the publisher.

Copyright © 2022 Berden, Piola and Palma. This is an open-access article distributed under the terms of the Creative Commons Attribution License (CC BY). The use, distribution or reproduction in other forums is permitted, provided the original author(s) and the copyright owner(s) are credited and that the original publication in this journal is cited, in accordance with accepted academic practice. No use, distribution or reproduction is permitted which does not comply with these terms.